universität wien

MASTERARBEIT / MASTER'S THESIS

Titel der Masterarbeit / Title of the Master's Thesis

„Focal parameters of a brightness optimised type-II Sagnac-based entangled photon-pair source“

verfasst von / submitted by

Jan Karl Lang, B.Sc.

angestrebter akademischer Grad / in partial fulfilment of the requirements for the degree of

Master of Science (MSc)

Wien, 2021 / Vienna, 2021

Studienkennzahl lt. Studienblatt / degree programme code as it appears on the student record sheet:	UA 066 876
Studienrichtung lt. Studienblatt / degree programme as it appears on the student record sheet:	Masterstudium Physik UG2002
Betreut von / Supervisor:	Univ.-Prof. Dr. Anton Zeilinger

Zusammenfassung

Ziel dieser Masterarbeit ist es, eine Quelle mit einer hohen Helligkeit von Photonenpaaren zu erreichen, ohne dabei zu viele einzelne Photonen zu erzeugen. Ausgangspunkt dieser Masterarbeit ist das Rauschresistente hochdimensionale nicht-lokale Interferenzexperiment, das bereits im Labor durchgeführt wurde [1]. Für die Erweiterung auf eine optischen Freiraumkommunikationslink über 10km benötigt die Photonenpaarquelle ein Upgrade. Um die verwendete Photonenpaarquelle vom Typ II mit einem Kristall von 30mm zu optimieren, werden die Kopplerlinsen variiert.
Die Helligkeit für einzelne Photonen beträgt $B_{\text{singles}} = (252 \pm 13) \cdot 10^3/(\text{mW}\cdot\text{s})$. (Definitionen in Section 3.2) Dies ist die maximale Grenze für die Einzelphotonenrate im gesamten Setup. Dadurch wird auch die höchste Helligkeit für Photonenpaare mit $B_{\text{pair}} = (65,6 \pm 3,6) \cdot 10^3/(\text{mW}\cdot\text{s})$ erreicht. Das Heralding ist dabei $\eta_{\text{Avg}} = (26,04 \pm 0,59)\%$. Ein zweites Paar Linsen konnte auch mit einem höheren Heralding von $\eta_{\text{Avg}} = (30,4 \pm 0,62)\%$ gefunden werden. Die Helligkeit beträgt für dieses Linsenpaar jedoch nur $B_{\text{pair}} = (59,5 \pm 3,3) \cdot 10^3/(\text{mW} \cdot \text{s})$. Da die verfügbare Leistung in der Quelle auf $28,5$mW begrenzt ist, erzeugt das andere Linsenpaar mehr Photonenpaare. (Tabellarische Gesamtübersicht siehe S.45)
Die verwendete Theorie [2] zur Optimierung der Helligkeit in der Quelle ist in guter Übereinstimmung für das gemessene Heralding. Für die Helligkeit hingegen ist die Theorie nur eine gute Näherung, wo das Maximum gefunden werden kann. Das Steigungsverhalten der theoretischen Helligkeitskurven stimmt dabei gut mit den tatsächlich beobachteten Werten überein. Für beide Linsenpaare liegt die Visibility in HV- und DA-Polarisation (siehe Section 1.1.2) über $99,0\%$. Diese Visibilitys für das hellere Linsenpaar sind für die Dauer von mindestens 72h langfristig stabil, wenn dazugehörge thermisch ungeschützte Fasern neu abgeglichen werden. Ansonsten nur für mindestens 24h. Dadurch fallen die Visibilitys nicht unter 96%. Ein kleinerer Fokus mit dem Pumplaser im Kristall hatte eine schlechtere Visibility von 2% zur Folge. Ein Bell-Test (siehe Section 1.1.3) beweist die Erzeugung maximal verschränkter Zustände. Die S-Werte sind $S = 2,81539 \pm 0,00064$ für das hellere Linsenpaar und $S = 2,81106 \pm 0,00027$ für das Heralding-effizientere Linsenpaar. Dies ist eine Verletzung der CHSH-Ungleichung von über 3000 Standardfehlern.
Die Quelle befindet sich dabei im spektral entarteten Zustand mit einer Wellenlänge der spontanen parametrisch herunterkonvertierten Photonen mit $\lambda_{\text{SPDC}} = 808,842$nm in einem und $\lambda_{\text{SPDC}} = 808,827$nm im anderen Arm der Typ-II-Quelle. Dies sind die Wellenlängen, die bei einer Temperaturabhängigkeit von $0,2$nm/K und einer Temperaturgenauigkeit von $0,1$K, am nähsten zusammenliegen.
Diese Masterarbeit hat ihr Ziel erreicht, eine Photonenpaarquelle vom Typ II mit einem Kristall von 30mm Länge aufzubauen, die möglichst viele Photonenpaare erzeugt. Durch die Gesamtoptimierung der Fokusparameter ist die Quelle um den Faktor 6 heller als die zuvor verwendete Quele bei der Durchführung im Labor [1] und hat es ermöglicht, das Rauschresistente hochdimensionale nicht-lokale Interferenzexperiment über einen Freiraumkommunikationslink und nicht nur im Labor durchzuführen.

Abstract

This master thesis accomplished a way to build a bright narrow bandwidth type-II photon pair source with a crystal of 30mm length. To optimise the source the coupler lenses are exchanged for generating a source with a high photon pair brightness without creating too many single photons. This requirements are retrieved from the noiseresilient free-space high dimensional non-local interference project where one part is close to the source and the other part is 10km away. This experiment was already carried out just in the laboratory [1] and the source needed an upgrade for the extension to the free-space link.
The brightness is $B_{\text{singles}} = (252 \pm 13) \cdot 10^3/(\text{mW} \cdot \text{s})$ for single photons which is the limit for the maximal acceptable single photon rate in the setup. (definition in section 3.2) Thereby also the highest brightness for photon pairs is achieved with $B_{\text{pairs}} = (65.6 \pm 3.6) \cdot 10^3/(\text{mW} \cdot \text{s})$. The heralding is $\eta_{\text{Avg}} = (26.04 \pm 0.59)\%$. A second pair of lenses is also found with a higher heralding of $\eta_{\text{Avg}} = (30.4 \pm 0.62)\%$ and can therefore serve as an alternative use for the source. The brightness is just $B_{\text{pairs}} = (59.5 \pm 3.3) \cdot 10^3/(\text{mW} \cdot \text{s})$for this lens pair. Because the available power inside the source is limited to 28.5mW the other lens pair produces more photon pairs. (Overview on p.45)
The theory[2] used to optimize the brightness in the source is a good prediction for the heralding. The theory for the brightness itself is only a good approximation where the maximum could be found. The trend of the theoretical brightness curves matches well with the actually observed values. For both lens pairs the visibility in HV and DA polarization (see section 1.1.2) is over 99.0%. This visibilities for the brighter lens pair are long term stable for at least the duration of 72h when involved exposed fibers become realigned or for at least over 24h. Thereby the visibilities do not drop below 96%. A stronger focus into the crystal with the pump laser had a 2% worse visibility as a result. A Bell test (see section 1.1.3) proves the generation of maximally entangled states. The S-values are $S = 2.81106 \pm 0.00027$ for the brighter lens pair and $S = 2.81539 \pm 0.00064$ for heralding efficient lens pair. This is a violation of the CHSH inequality of over 3000 standard errors.
The source is thereby in the spectral degenerate case with a wavelength of the spontaneous parametric down converted photons with $\lambda_{\text{SPDC}} = 808.842$nm in one and $\lambda_{\text{SPDC}} = 808.827$nm in the other arm of the type-II source. These are the closest wavelengths corresponding to temperature dependency of 0.2nm/K and a temperature accuracy of 0.1K.
Through the overall optimisation of the focal parameters the source is a factor 6 brighter than the source in just the laboratory experiment [1] and so it was possible to carry out the noiseresilient high dimensional non-local interference experiment over a free-space of 10km and not just only in the laboratory.

Contents

Chapter 1

Introduction

The goal of this master thesis was to build a bright narrow bandwidth photon pair source. This source was used to investigate the nature of noise in higher dimensional entangled time energy quantum states in a real world scenario where the narrow bandwidth is a requirement. The high dimension entanglement in energy-time has in the laboratory already been proven that it is much more resilient against noise than just polarization [1]. In order to show that it is not just possible to overcome noise in a laboratory environment the entire project is extended to an intra city free-space link. The requirement of a high brightness is introduced by the additional free-space link with the challenge of additional loss.
This work describes the improvement in the amount of generated photon pairs per used pump power of the previously existing source. The adjustment of the brightness is necessary because because the power of the pump laser is limited by the pump laser's wavelength stabilisation which is necessary for the narrow bandwidth source. In order to receive more photons through the lossy free-space channel it is therefore necessary to effectively create more pairs from the pump laser which increases the absolute amount of detectable photon pairs. The stabilisation is locked on a hyperfine structure transition line of potassium and becomes unstable for higher powers. The old source has a low brightness ($\sim 15 \cdot 10^3$ pairs/(s mW)) [1] and is the main goal for an improvement. The source shall simultaneously fulfill the additional requirements for the usage in time-frequency entanglement as well as polarization entanglement.

The pathway to achieve this is described in this master thesis. Chapter 2 gives an outline of the entire project where the special requirements for the source are emphasized. The source shall have a high visibility in two linear polarized mutual unbiased bases, the same wavelength for both output arms, the maximum possible heralding and around seven million single photons per second in each output arm of the source. This requirements are determined from the different components of the entire project.
Chapter 3 describes the working principle of the used Sagnac source template, the actual used implementation in the setup and the values which are used for the source's characteristica. In order to generate more photon pairs from the source the focus parameters of the actual source need to be changed. The goal is to find the point at which the maximum possible number of photons can be coupled in without significantly worsening the produced state. The approach to achieve a brightness optimised source is the theory of Bennink [2]. His theory is in good agreement with Fedrizzi [3] and Steinlechner [4] already practically performed measurements for longer crystals. The maximum length used from those authors are just 25mm. The now

used crystal has a length of 30mm which makes a characterisation of the focal parameters necessary.
This characterisation is made in Chapter 4. Thereby a consistent alignment method had to be found so that the source can be quickly made operational again in the case of a possible misalignment. A set of lenses is found which fulfill all requirements in brightness, wavelength and quantum mechanical state of the source. The quantum mechanical nature of a maximally entangled state is proven with a Bell test (Section 4.2.3) and the stability of the source is suitable for long term measurements in the regime of days (Section 4.3.1).

This upgraded source contributes a major milestone to the project which tries to overcome noise in entanglement distribution. The much higher brightness in the source made an alignment of the two 10km apart interferometers with high enough count rates for real time alignment possible.

1.1 Fundamental concepts

1.1.1 Gaussian beam

The Gaussian beam optics is the conjunction between geometrical optics and wave optics. It is derived from the Maxwell equations with the absence of charged particles. The result is a wave equation for the electromagnetic field $\mathbf{E}$

$$c^2 \Delta \mathbf{E}(\mathbf{r}, t) = \ddot{\mathbf{E}}(\mathbf{r}, t) \tag{1.1}$$

where c is the speed of light, $\mathbf{r}$ is the position and t the time. By using a cylindrical coordinate system the equation can be solved with a propagation in the z-direction and a transverse profile in the xy-plain. Solving this equation in zero-order for x and y, x and y are summarized as the radial component r and the solution is the so called fundamental transverse Gaussian mode TEM_{00}. The solution for the intensity $I(r, z)$ is

$$I(r, z) = I_0 \left(\frac{w_0}{w(z)} \right)^2 \mathrm{e}^{-\frac{2r^2}{w(z)^2}} \propto |E(r, z)|^2 \tag{1.2}$$

where I_0 is intensity at the center of the beam at its waist, w_0 is the minimal beam waist and $w(z)$ is the beam waist at position z. This is a two dimensional radial Gaussian distribution. The beam waist is defined as

$$w(z) = w_0 \cdot \sqrt{1 + \left(\frac{z}{z_R} \right)^2} \tag{1.3}$$

with the Rayleigh range $z_R = \pi \cdot w_0^2 / \lambda$ and the wavelength of the light λ. These quantities can be seen in Figure 1.1. z_R is thereby also defined as $w(z_R) = \sqrt{2} w_0$ where the beam area is doubled. The beam waist for far away distances becomes in the limit a linear function $\lim_{z \to \infty} \omega(z) = \frac{\omega_0}{z_r} \cdot z$. This provides the possibility to define a divergence angle $\theta_{\mathrm{div}} =$

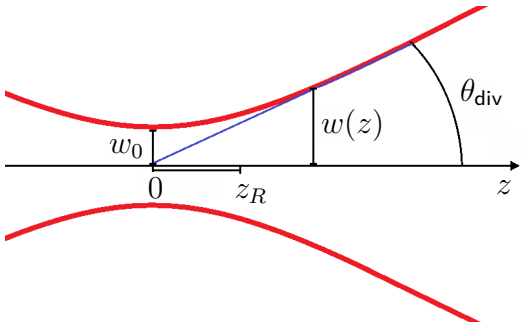

Figure 1.1: Beam waist of Gaussian beam (red). The minimal beam waist ω_0, the Rayleigh range z_R and the divergence angel θ_{div} are marked.

$\arctan(w(z)/z)$ which stays constant for distances $z \gg z_R$ as $\theta_{\text{div}} = \arctan(\lambda/(\pi \cdot w_0))$ [5, p.235ff].

This concept of the Gaussian beam can be connected with the end of a single mode fiber. A single mode fiber acts like the name implies as a waveguide for the fundamental transverse Gaussian mode TEM_{00}. At the tip of a single mode fiber $(z = 0)$ this propagation continues in very good approximation as a Gaussian beam with the minimal beam waist at the tip of the fiber. This beam waist w_0 at the tip of the fiber is normally given by the manufacturer with the mean field diameter ø_{fiber} which is twice the beam waist. To collimate a laser beam with a beam diameter of ø_{coll} an aspheric lens with focal length f is normally used to accomplish this. By using the concept that for $z \gg z_R$ the Gaussian beam acts just like geometric optics. This is possible as long $f \gg z_R$. In this case the diameter of the collimated beam

$$\text{ø}_{\text{coll}} = 2 \cdot w(f) = 2 \cdot \frac{w_0}{z_R} \cdot f = \frac{4 \cdot \lambda \cdot f}{\pi \cdot \text{ø}_{\text{fiber}}} \tag{1.4}$$

can be expressed as twice the beam waist at the focal length of the used collimation lens. Rewriting this equation with known relations gives a short term for the collimated beam diameter in dependency of the wavelength λ, the focal length f and the mean field diameter ø_{fiber} of the fiber tip. This leads to a larger Rayleigh range

$${z_R}' = \frac{4 \cdot \lambda \cdot f^2}{\pi \cdot {\text{ø}_{\text{fiber}}}^2} = \frac{f^2}{z_R} \tag{1.5}$$

after the collimation lens where the minimal beam waist for the collimated beam is in the plane of the lens $(z' = 0)$. For $z' \ll {z_R}'$ the beam waist can be assumed as constant and also the diameter of the collimated beam.

1.1.2 Polarization

Polarization of light is described by the orientation of the electromagnetic field's oscillation in the transverse plain. The most media present - like air - are polarization maintaining so using quantum states with polarization as information carrier is a well known and used way in quantum communications. In polarization exist three independent set of bases. Two of them

are linear the HV and DA polarization and the circular polarization RL. H is the horizontally polarized light and V is the orthogonal polarization called vertically polarized light. The second basis set of linear polarized light DA is $45°$ rotated corresponding to the HV basis. D is thereby called diagonal and the orthogonal polarization A anti-diagonal. The third basis set is the circular polarization where the name already implies that the polarization is rotating in a circle. R is thereby the right-handed circular polarization and L the orthogonal left-handed circular polarization. In terms of the two dimensional computational bases $|0\rangle$ and $|1\rangle$ the polarization of single photons can be expressed in one of the three polarization bases as:

$$\text{HV-basis}: \quad |H\rangle = |0\rangle = \begin{pmatrix} 1 \\ 0 \end{pmatrix}, \qquad |V\rangle = |1\rangle = \begin{pmatrix} 0 \\ 1 \end{pmatrix} \tag{1.6}$$

$$\text{DA-basis}: \quad |D\rangle = \frac{1}{\sqrt{2}} \begin{pmatrix} 1 \\ 1 \end{pmatrix}, \qquad |A\rangle = \frac{1}{\sqrt{2}} \begin{pmatrix} 1 \\ -1 \end{pmatrix} \tag{1.7}$$

$$\text{RL-basis}: \quad |R\rangle = \frac{1}{\sqrt{2}} \begin{pmatrix} 1 \\ \mathrm{i} \end{pmatrix}, \qquad |L\rangle = \frac{1}{\sqrt{2}} \begin{pmatrix} 1 \\ -\mathrm{i} \end{pmatrix} \tag{1.8}$$

Each basis can be expressed in terms of each other's basis set. These orthogonal basis vectors are eigenvectors of their corresponding measurement operators.

$$\sigma_{\mathsf{HV}} = \begin{pmatrix} 1 & 0 \\ 0 & -1 \end{pmatrix}, \quad \sigma_{\mathsf{DA}} = \begin{pmatrix} 0 & 1 \\ 1 & 0 \end{pmatrix}, \quad \sigma_{\mathsf{RL}} = \begin{pmatrix} 0 & -\mathrm{i} \\ \mathrm{i} & 0 \end{pmatrix} \tag{1.9}$$

In the matrix representation the measurement operators are the Pauli matrices. Consequently these fulfill the Pauli commutation relations and the three bases are mutually unbiased in comparison to each other. To measure one specific linear polarization $P(\phi)$ for example with a polarisator at measurement angle ϕ where $\phi = 0$ is equal to H polarization. The corresponding measurement matrix is a projection in the polarization Bloch sphere with

$$P(\phi) = \frac{1}{2} \left(\mathbf{1} + \sigma_{\mathsf{HV}} \cos(2\phi) + \sigma_{\mathsf{DA}} \sin(2\phi) \right) \tag{1.10}$$

and $\mathbf{1}$ as the identity matrix. Applying this operator to a single photon is nothing else but the probability of the single photon passing through a polarisator at angle ϕ [6].

1.1.3 Entanglement

Every state $|\Psi\rangle$, which is consisting out of more than one subspace $\mathcal{H}_j$ with substates $|\psi_j\rangle$, is entangled if $|\Psi\rangle$ is not separable in all its subspaces.

$$|\Psi\rangle \neq \prod_j^{\otimes} |\psi_j\rangle \tag{1.11}$$

Separability means that every transformation or measurement applied to just one subspace has no effect to all other subspaces because every subspace's state has no interconnection

with all the other states in the different subspaces. Reverting this logic means that for an entangled state a transformation or measurement of just one subspace can affect the other subspaces states in a joint state. This is from the quantum mechanics perspective of view not limited by the relativistic information spreading boundary of light speed. Therefore it was assumed that quantum mechanics must not provide a complete description of reality and there has to be a set of hidden variables to get rid of unsatisfactory non-deterministic elements of quantum physics. This was proposed by Einstein, Podolsky and Rosen (EPR) in their famous EPR-paper [7].

The Bell states

For disproving the idea of local hidden variables Bell[8] proposed the first of the four famous Bell states with the spin singlet state. In the case of polarized photon each Bell state consists out two polarized photons each in a subspace $\mathcal{H}_1$ and $\mathcal{H}_2$.

$$|\phi^{\pm}\rangle = \frac{1}{\sqrt{2}} \left(|H\rangle_1 |H\rangle_2 \pm |V\rangle_1 |V\rangle_2 \right) \tag{1.12}$$

$$|\psi^{\pm}\rangle = \frac{1}{\sqrt{2}} \left(|H\rangle_1 |V\rangle_2 \pm |V\rangle_1 |H\rangle_2 \right) \tag{1.13}$$

The structure of the Bell states is directly showing the idea behind entanglement because measuring either the polarization of photon 1 or 2 already defining the outcome of the second measurement. If this would happen in just one of the mutual unbiased bases there would be no difference between the classical and the quantum mechanical case. In the classical case it would be also possible to prepare packages which have exactly these properties for just one polarization basis. If the classical case is then switched to a different base, this correlation in the measurement is vanished. In the quantum case this is not true because there the photon pairs represent simultaneously both combinations until a measurement.

CHSH inequality

From the idea of EPR and Bell Clauser, Horne, Shimony and Holt[9] (short CHSH) proposed an equation which allows an easy verification of the Bell inequality. The so called CHSH inequality has to hold

$$S = |E(\alpha, \beta) - E(\alpha, \beta')| + |E(\alpha', \beta) + E(\alpha', \beta')| \leq 2 \tag{1.14}$$

if the assumption of hidden variables are true. Thereby are α and α' the measurement settings of detector A, and β and β' of detector B. E is a measure for correlation

$$E(\alpha, \beta) = P_{\alpha\beta} + P_{\alpha_\perp\beta_\perp} - P_{\alpha\beta_\perp} - P_{\alpha_\perp\beta} \tag{1.15}$$

E only takes on the values from -1 to 1, 1 if they are fully correlated, -1 if anti-correlated and 0 if they or not correlated. The subscript $\perp$ indicates orthogonal bases. Extending

Equation (1.10) for a two dimensional Hilbertspace

$$P_{\alpha\beta} = P(\alpha) \otimes P(\beta) \tag{1.16}$$

where the polarization of both photons are independently measured. The later used source configuration is built to mainly produce the $|\psi^-\rangle$ Bell state. Applying therefore the operator $P_{\alpha\beta}$ to a $|\psi^-\rangle$ results in

$$\langle\Psi^-| P_{\alpha\beta} |\Psi^-\rangle = \frac{1}{2}\sin(\alpha-\beta)^2 \tag{1.17}$$

which can be used to calculate the Es by using the fact that the subscript $\perp$ are $\pi/2$ in terms of orthogonal polarization.

$$E(\alpha,\beta) = \sin(2\alpha + 2\beta) \tag{1.18}$$

To exceed the limit of 2 in Equation (1.14) for the S value a maximal violation is possible up to $S = 2\sqrt{2}$ [10]. For the violation of the CHSH inequality four bases are defined for α and β. HV for α and DA for α'. For β, B1 is defined with one polarization at $22.5°$ and the orthogonal polarization at $112.5°$, and for β', B2 with one polarization at $67.5°$ and the orthogonal polarization at $157.5°$. This set of bases is able to violate the CHSH inequality up to $2\sqrt{2}$ with a maximal entangled Bell state.

Possible loopholes in the Bell test

Already Bell pointed out that some aspects need additional attention in the whole measurement process. The most common loopholes of photonic bell tests are the locality/signaling, freedom of choice, detection efficiency/fair sampling and memory. These loopholes can introduce the possibility that the violation of the Bell inequality is done by a hidden variable. These loopholes can be closed to exclude the possibilities of the existence of such hidden variables.

Locality/Signaling: This loophole assumes that no space-time like separation is present. This allows an exchange of information without violating the maximal speed for communication - the speed of light. The detectors need to be space-time like separate to avoid the communication between both detectors. This separation has to be chosen in the way that no signal of the basis choices or the measured photons can reach an other party [11].

Freedom of choice: This loophole addresses the assumption that the basis choices of both measurement parties are independent. Otherwise it opens the possibility of a hidden variable which can influence the basis choice. This leads to the point that the basis has to be chosen space-time delayed corresponding to the other measurement party [11].

Detection efficiency/Fair sampling: The fair sampling assumption uses the detected subensemble as a representative of the entire ensemble of the detected photons. This creates the possibility of a loophole such that just the subensemble is violating the Bell inequality. Therefore the CHSH inequality has to take the detection efficiency into account [12].

Memory: The measurement outcome could be influenced by the memory of the used measurement devices because the memory could know the necessary statistic to predict a possible violation [13].

1.1.4 SPDC process

Spontaneous Parametric Down-Conversion (SPDC) is a non-linear process, in which photons from a pump beam (index p) are spontaneously split into a pair of photons of lower frequencies (index 1, 2) while propagating through a non-linear medium. This process is called an $\chi^{(2)}$-process. The name comes from the second quantised Hamiltonian

$$\hat{H} = \hbar\omega_p \hat{a}^\dagger_{\omega_p}\hat{a}_{\omega_p} + \hbar\omega_1 \hat{a}^\dagger_{\omega_1}\hat{a}_{\omega_1} + \hbar\omega_2 \hat{a}^\dagger_{\omega_2}\hat{a}_{\omega_2} + \chi^{(2)}_{\text{eff}}\left(a^\dagger_{\omega_1}a^\dagger_{\omega_2}a_{\omega_p} + a^\dagger_{\omega_p}a_{\omega_1}a_{\omega_2}\right) \tag{1.19}$$

where $\chi^{(2)}_{\text{eff}}$ is the approximation in second order for a polarizable medium. The $\hat{a}_\omega$ and $\hat{a}^\dagger_\omega$ are the so called creation and annihilation operators with frequency ω for the different photons. These photons can also have different kind of polarization corresponding to each other. The first three terms are simply speaking just the living condition for the three different kind of photons. The important last term is the so called SPDC term where a photon of the pump beam gets annihilated and two photons are created. This process works also vice versa because of the needed hermitian of the Hamiltonian. The two created photons are conserving energy with $\omega_p = \omega_1 + \omega_2$ and also inherit their phase from the pump photon [14]. The conservation of momentum $\mathbf{k}_p = \mathbf{k}_1 + \mathbf{k}_2 + \Delta\mathbf{k}$ is guaranteed with the phase miss match of $\Delta\mathbf{k}$ which can be compensated with a poling period Λ of the used crystal with $\Delta k = 2\pi/\Lambda$. For the collinear case which is achieved by bidirectional pumping in the Sagnac interferomter scheme the propagation orientation of all $\mathbf{k}$ are equal and can thereby expressed as just k. Expressing k with $k = n_P(\omega)\omega/c$ with $n_P(\omega)$ the refractive index of a certain polarization P inside the crystal for the specified frequency. The conservation of energy can be used to determine the poling period for a given pump frequency ω_p and the condition that $\omega_1 = \omega_2$ for the degenerate case in a type-II crystal as

$$\Lambda = \frac{4\pi \cdot c}{\omega_p \cdot (2 \cdot n_{\mathsf{H}}(\omega_p) - n_{\mathsf{H}}(\omega_p/2) - n_{\mathsf{V}}(\omega_p/2))} \tag{1.20}$$

This means that the quasi phase matching condition just holds for a specified wavelength. There are existing three different types of SPDC-processes corresponding to the polarization of the outcoming photons if the pump photon is H-polarized [15, p.79ff]:

- Type-0: The SPDC photons are both H-polarized
- Tpye-I: The SPDC photons are both V-polarized
- Type-II: One SPDC photon is H-polarized and the other on is V-polarized

In this master thesis a type-II 30mm long periodically poled potassium titanyl phosphate (ppKTP) crystal is used. It has the refractive index for the pump laser wavelength $n_{p,\mathsf{H}} = 1.865$ and for the SPDC photon pairs in the degenerate case $n_{\text{SPDC,H}} = 1.761$ and $n_{\text{SPDC,V}} = 1.887$ for a temperature of $45°$C [16, 17]. This values are just an approximation for 404.5nm because the given Sellmeier equations hold just down to 430nm. The poling period is $\Lambda = 9.86\mu$m and is thereby phase matched for 404.5nm. Comparing this with the refractive indices gathered by the Sellmeier equation Equation (1.20) gives $\Lambda_{\text{calc}} = 9.85\mu$m. This is good hint that the Sellmeier equations give at least a useful approximation for the refractive indices of the used crystal.

Chapter 2

Noiseresilient free-space high dimensional non-local interference

This chapter provides a brief outline of the project for which the source is built for and describes the requirements and the parameters which are available for optimisation. Therefore it is not explaining the exact protocol and working principle of the project itself (see [1, 18]). It just points out the technical realisation and its limits.

2.1 Photons' degrees of freedom

The basic requirement for the protocol is a hyper entangled state $|\Psi\rangle$. Therefore it is necessary to use more than just one degree of freedom of a photon. For SPDC-photons the degrees of freedom in polarization, spatial modes and energy-time are available [19]. Because the degree of freedom in energy-time is entangled for free in the SPDC process [20] a hyper entangled state in polarization and energy time is used for the protocol.

$$|\Psi\rangle = |\Phi\rangle_{\text{pol}} \otimes |\Phi\rangle_{\text{energy-time}} \tag{2.1}$$

2.1.1 Polarization entanglement

For polarization a maximally entangled Bell state is prepared. The source provides thereby a $|\Psi^{\pm}\rangle$ Bell state. A type-II Sagnac source is intrinsically producing this state. For the Franson protocol is a symmetric $|\Phi^{\pm}\rangle$ Bell necessary. This is achieved by the usage of a fiber transformation U where the unitary transformation in one of the two fibers is not aligned as a unitary identity which is normally done. Instead the one fiber is oriented such that the orthogonal polarization in HV are interchanged with a Bitflip σ_{DA} (see eq. (1.9)). With this unitary transformation the

$$U\,|\Psi^{\pm}\rangle = (1 \otimes \sigma_{\text{DA}})\,|\Psi^{\pm}\rangle = |\Phi^{\pm}\rangle \tag{2.2}$$

state of the source can be flipped to the desired Bell state.

2.1.2 Time-bin entanglement

The SPDC process creates - by sustaining the law of energy conservation - out of one pump photon with the defined energy $\hbar\omega_p$ two photons with the energy $\hbar\omega_1$ and $\hbar\omega_2$. This results in $\omega_p = \omega_1 + \omega_2$. The total energy is strictly conserved such that the frequency bandwidth $\Delta\omega$ of the photon pairs resulting in a high entangled state because $\omega_p = (\omega_1 \pm \Delta\omega) + (\omega_2 \mp \Delta\omega)$ where $\Delta\omega$ is normal distributed. By using $\Delta\omega_{\text{FWHM}}$ of this distribution the coherence time τ can be expressed as $\tau = 2\pi/\Delta\omega_{\text{FWHM}}$. Coherence time and bandwidth are inversely related which means that a narrower pump bandwidth results in a longer coherence time for the emitted photon pairs. This results in an entanglement in the time domain where $a^\dagger(t_1)$ and $a^\dagger(t_2)$ are the creation operators at the creation time t_1 and t_2. The resulting state $|\Phi\rangle_{\text{energy-time}}$ with energy-time entanglement can be expressed as

$$|\Phi\rangle_{\text{energy-time}} = \int \mathrm{d}t_1 \, \mathrm{d}t_2 \, g(t_1, t_2) \, a^\dagger(t_1) \, a^\dagger(t_2) \, |0\rangle \tag{2.3}$$

where $g(t_1, t_2) \to 0$ is a normalized function that becomes zero for $|t_1 - t_2|$ sufficiently large [21]. By the assumption that $|t_1 - t_2| < \Delta t$ where $g(t_1, t_2)$ becomes zero and Δt is the used bin size. The minimal Δt is in this experiment limited by the technical realisation of the measurement device. Because the minimal used Δt interfere not with the normalized function the continuous integral can be expressed as a sum and the state in energy time can be approximated as a time bin state $\Phi_{\text{time-bin}}$

$$|\Phi\rangle_{\text{energy-time}} \approx \Phi_{\text{time-bin}} = \frac{1}{\sqrt{N}} \left(\sum_{j=1}^{N} |j \cdot \Delta t\rangle_1 \, |j \cdot \Delta t\rangle_2 \right) \tag{2.4}$$

In the case that a continuous wave laser is used the probability for all bins are equal. From a theoretical point of view this spans an infinite dimensional state with dimension N. For a realistic technical realisation this experiment is limiting the dimension to d to create a time frame of $F = d \cdot \Delta t$ where the bins inside just simply labeled with an integer number.

$$\Phi_{\text{time-bin}} = \frac{1}{\sqrt{d}} \left(\sum_{j=1}^{d} |j\rangle_1 \, |j\rangle_2 \right) \tag{2.5}$$

From an intuitive perspective the description of this state is clear because it simply says if you do not look super exactly at the creation time - the approximation to time bins - the photons get created in pairs randomly in the time domain.

2.2 Advantages of the protocol

The main advantage of the protocol is the usage of an additional degree of freedom than just polarization. The degree of freedom used in addition is generated naturally in the SPDC process. So it is not necessary to make an extra effort to generate a state with an additional degree of freedom. Because quantum states are losing there encoded information with the slightest interaction with the environment long distance communication need special noise robust protocols. That noise limiting the information transfer is the same in the classical communication field, but there the problem can just simply solved by sending many times the same information. This is not possible for quantum states because of the effect of the non cloning theorem [6, p.586ff].
To overcome the noisy environment in the two-level system of polarization a higher dimensional space is used to increase the robustness to noise. This is accomplished by using the higher dimensional space in the time domain which is discretized in the form of time bins. This is possible because in higher dimension it is easier to distinguish between noise and actual measured quantum state. The dimension affects also the final generated key because for higher dimension more values have to be discarded in the post-processing. This results in the effect that higher dimensions can still create a secure key where a quantum two-level system is not able anymore. But increasing the dimension add also additional noise so the sweet spot has to be found. By changing the dimension between day and night it can be taken care of different noise levels [1]. The main noise is thereby caused by the sun during the day.
The protocol makes it possible to overcome noise as long the photon arrives at its desired destination. But it is not possible to overcome rain or fog which are just additional attenuation.

The main goal of the in the next section introduced experiment is to give a proof of principle of the protocol in a realistic environment. This shall demonstrate that a future application in quantum communication in a satellite-ground scenario is possible. This master thesis contributes a highly specialised source to the experiment where the requirements for the source (see section 2.4) are derived from the other components in the entire experiment.

2.3 Setup

Each part later will be explained in great detail individually. The entire setup of the project is shown in Figure 2.1. The setup is divided physically by a 10km free-space link in the

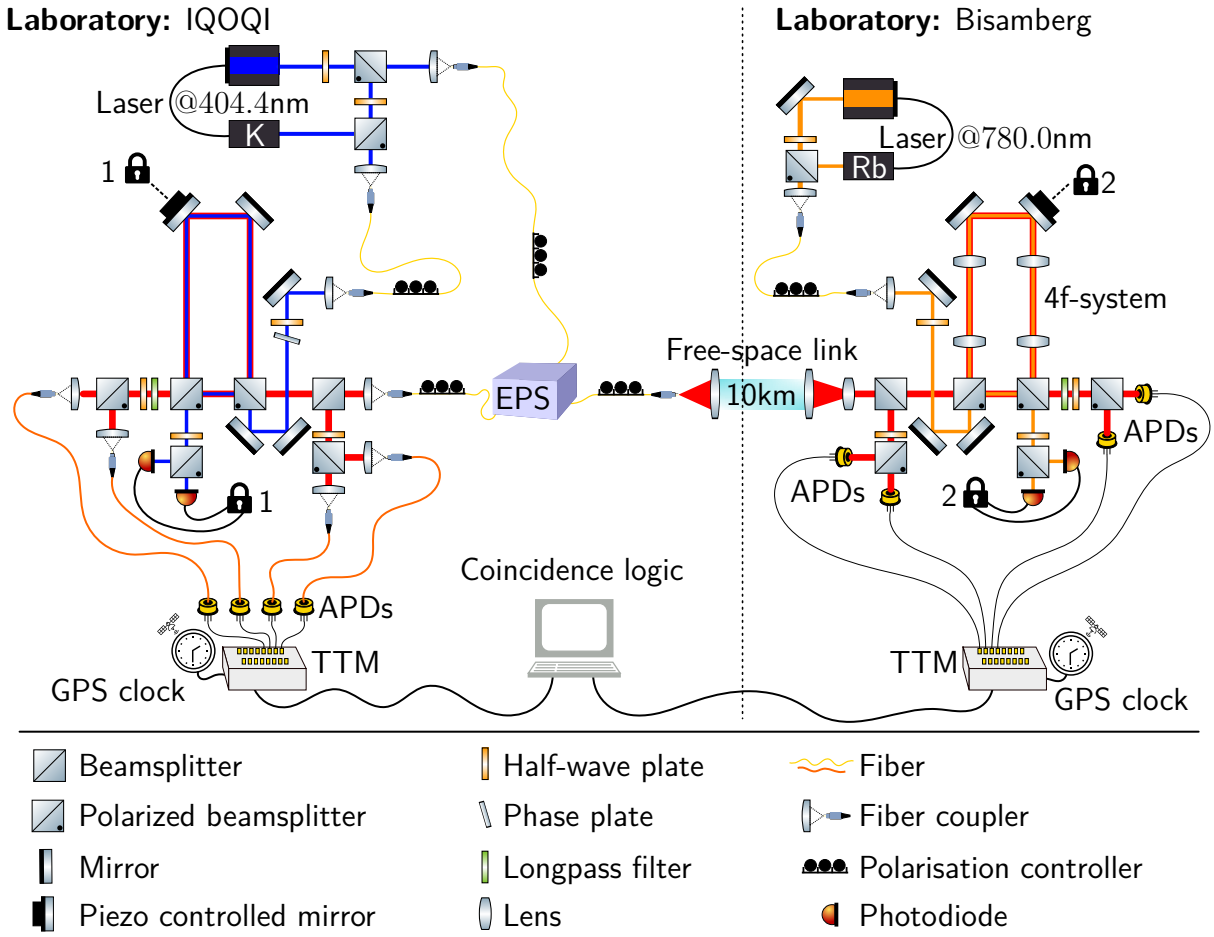

Figure 2.1: Schemata of the entire setup with explanation in the text.
Potassium stabilized laser (blue), Rubidium stabilized laser (orange), SPDC photons (red), entangled photon pair source (EPS), avalanche photo diodes (APDs), time tagging modules (TTM) synchronized with GPS, single mode fiber (yellow), multi mode fiber (orange)

city Vienna between the laboratory inside the *Institute for Quantum Optics and Quantum Information Vienna* (*IQOQI*) and the laboratory on the hill *Bisamberg*. The different parts in the setup are the UV pump and stabilisation laser (blue), the IR stabilisation laser (orange), the entangled photon pair source (EPS), the free-space link, two similar measurement setups in each laboratory for the single photons (red), the detection with avalanche photo diodes (APDs) connected to GPS synced time tagging modules (TTM) and a coincidence logic to detect photon pairs. These parts are individually explained in the following Sections 2.3.1 to 2.3.3. The parts are connected with single mode fibers (yellow) and polarization controllers to maintain the polarization after the fiber. Free-space link, measurement and protocol are not the main topic of the thesis. Each of them are discussed in high detail in separate works. The following sections just introducing briefly the working principle and giving necessary information for the requirements of the source.

2.3.1 Free-space link

The 10km free-space link shown in Figure 2.2 is established with a sender module at the *IQOQI* and a receiving module at the *Bisamberg*. From experimental tests done before the attenuation

Figure 2.2: Satellite picture of Vienna from the free-space link of 10km between sender (*IQOQI*) and receiver (*Bisamberg*).

over the free-space link is between 20dB to 25dB. This is caused by the unavoidable effects of absorption and scattering in the atmosphere. Also fluctuations in the temperature and pressure are causing changes of the atmospherics's density and so the refractive index. For a 10km free space link it is not unlikely that temperature and wind change the density of the atmosphere and cause beam wander and wave front distortion. By accomplishing two way tracking with 532nm light long term instabilities can be compensated [22]. For measurements during the day we are placing additional narrow filters after the free-space link in the *Bisamberg* laboratory to filter out stray light photons from the sun. Therefore the photons from the source need to have a small spectral line width to filter out as many unwanted photons as possible. With the used filter is the typical count rate of detected photons in one detector contributed by the sun $\sim 1 \cdot 10^6$/s counts.

2.3.2 Measurement and Analysis

In each laboratory the measurement is done in two different bases. A beamsplitter provides thereby the passive bases choice. In one arm the state is measured in the DA polarization basis. In the other arm the state is measured in the time domain with a Franson interferometer. The passive bases choice is necessary to give a security proof for the possible application in quantum key distribution [18]. The photons are detected with single photon counting modules which are highly advanced avalanche photo diodes and afterwards digitised with a time tagging module. The time tagging module is synchronised with an atomic Rubidium clock disciplined by 10kHz GPS signal. The GPS also provides a 1Hz-signal which is used to synchronise the time tagging modules in each laboratory as a start signal. The data of both time tagging modules is send via network to a computer which evaluates the coincidences and determines the visibilities [23].

Franson interferometer

The first suggestion to violate the Bell inequality also in energy-time was made by Franson[24]. His idea was quickly extended to post-selection free Franson interferometer [25]. This requires a hyper entangled state in polarization and energy-time in the form of Equation (2.1). The post-selection free Franson interferometer replaces the beamsplitter in the Franson interferometer with a polarized beamsplitter. The usage of $|\Phi^{\pm}\rangle$ Bell states in polarization for the post-selection free Franson interferometers neglects all terms where the photon in one interferometer enters the short arm and the photon in the other interferometer enters the long arm or vice versa. To remove the measurement information in the basis of the polarized beamsplitter (HV) the final measurement basis is in a mutual unbiased basis (DA) corresponding to those of the polarized beamsplitter. This is accomplished by a half-wave plate before the final measurement at $22.5°$.
In the domain of time bins $|j\rangle_1 |j\rangle_2$ photons can either pass both the short path in the interferometer or both the long path with the additional delay f. This results in the state

$$\frac{1}{\sqrt{2}} \left(|j\rangle_1 |j\rangle_2 + e^{\mathrm{i}\phi_\mathsf{F}} |j+f\rangle_1 |j+f\rangle_2 \right) \tag{2.6}$$

where ϕ_F is the sum of the phases of both interferometers. By combining this with the usage of polarized beamsplitters and an adjustable pump phase ϕ_p in the polarization state $|\Phi\rangle_{\mathsf{pol}}$ the state $|\Psi\rangle_{\mathsf{out}}$ after the Franson interferometer in the mutual unbiased basis DA is

$$\begin{aligned} |\Psi\rangle_{\mathsf{out}} = \Bigg[& \cos\left(\frac{\phi_\mathsf{F}+\phi_p}{2}\right) \left(|D\rangle_1 |D\rangle_2 + |A\rangle_1 |A\rangle_2 \right) \\ & + \mathrm{i}\sin\left(\frac{\phi_\mathsf{F}+\phi_p}{2}\right) \left(|D\rangle_1 |A\rangle_2 + |A\rangle_1 |D\rangle_2 \right) \Bigg] \otimes \frac{1}{\sqrt{d}} \sum_{j=1}^{d} |j\rangle_1 |j\rangle_2 \end{aligned} \tag{2.7}$$

where $j+f$ can be relabeled to j through the repeating time frames of length d. The Franson visibility is the contrast between the photon pairs with identical polarizations and opposite polarizations and depends on the interferometer phase and the adjustable pump phase.
By changing the relative phase of the stabilisation laser the phase ϕ_F can be adjusted with the phase plate in the *IQOQI* laboratory. In the measurement in DA basis the additional phase ϕ_F appears in the end. By setting up the phase correctly the state can be adjusted in the way that the Franson visibility is maximal [25].
In the Franson interferometer at the *Bisamberg* an additional 4f-system is placed which increases the angles of view over the free space link and so the working capacity of the interferometer. The 4f-system consist out of four lenses with shared focal points. This compensates short term fluctuations over the free-space link [26].

2.3.3 Pump laser

The photon pair source is pumped with a narrow-band laser [27, 28]. For creating an ultra narrow line width laser a Doppler free absorption spectroscopy is used to lock the laser on a hyperfine structure line of Potassium so the spectrum of the laser wont change. This is the

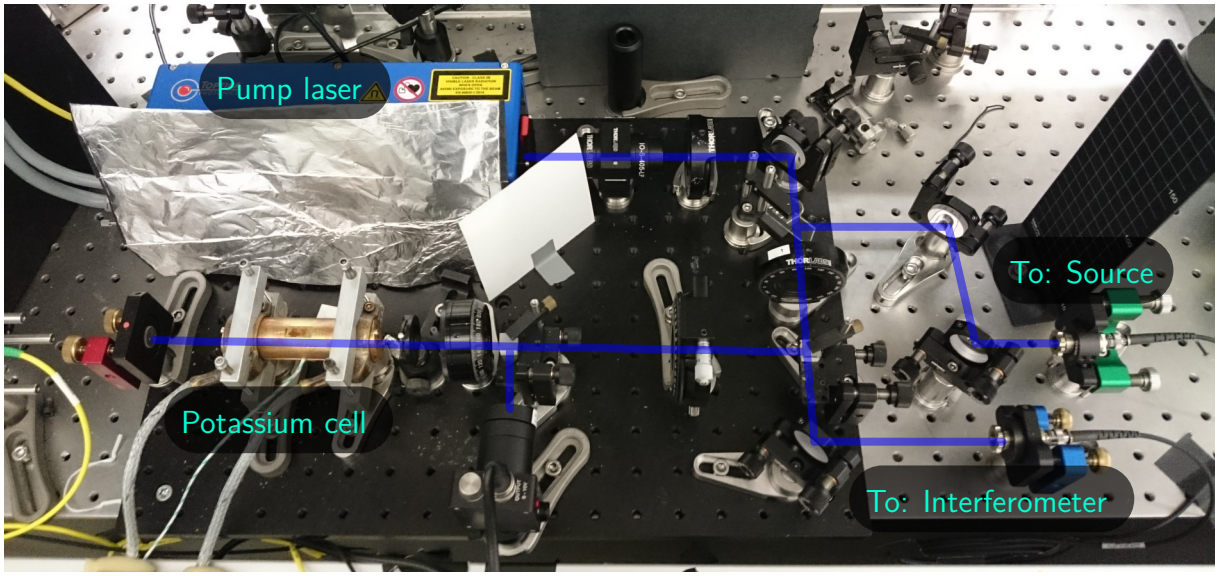

Figure 2.3: Pump laser with a Potassium cell for a Doppler-free spectroscopy to lock the laser on a hyperfine structure line and the two branches towards the entangled photon pair source (incoming power ~ 80mW) and the Franson interferometer (incoming power ~ 10mW). The power ratios are adjusted with half-wave plates and polarized beamsplitters.

reason why the the pumping power is limited because the used method has to possibility of irreversible drifts. This possibility highly rises a certain laser power which is around ~ 100mW. The used setup is shown in Figure 2.3 where the power is branched off for the interferometer stabilisation and the entangled photon pair source. The Potassium cell is heated up. These atoms are used to lock the laser on the transition line with an energy difference of $\Delta E = 3.0658$eV which corresponds to a wavelength in air of $\lambda = 404.414$nm [29]. (A complete description can be found in future published work of Kohout [30].)

2.4 Requirements for the source

The entire setup introduces thereby two different specification requirements through the free-space link. On the *Bisamberg*-side enough photons shall be detectable to overcome the attenuation of the free-space link. Guessing the effect of lost on the *Bisamberg*-side with ≈ 30dB and assuming for the possibility of a real-time evaluation a pair rate of $1 \cdot 10^3$/s. A pair creation rate of at least $1 \cdot 10^6$/s are wanted directly from the source. This leads to the requirement of a high photon pair count rate and therefore a bright source. On the *IQOQI*-side very high single photon count rates are leading to a saturation of the detectors and the detectors will lose their exact time resolution. This caused by non-linearity effect of the used detectors in the regime of high count rates. The direct detectable single photon rate should not exceed $7 \cdot 10^6$/s of each output from the source (see section 4.1.1). This is combined with the fact that the pump laser power is strictly limited. Therefore the source is desired with as many photon pairs as possible per detected photon and pump laser power. This ensures that no detectors get saturated and a real-time evaluation of the Franson visibility is possible.
The selected source setup is a Sagnac setup and produces the maximal entangled Bell state $|\Psi^{\pm}\rangle$ where the relative phase can be easy adjusted. Additionally the created photons need

to have a small spectral line width for the additional entanglement in time and the daylight usage. The source need to produce the state

$$|\Psi\rangle = \frac{1}{\sqrt{2}} \left(|H\rangle_1 |V\rangle_2 + e^{\mathrm{i}\phi} |V\rangle_1 |H\rangle_2 \right) \otimes \frac{1}{\sqrt{d}} \left(\sum_{j=1}^{d} |j\rangle_1 |j\rangle_2 \right) \tag{2.8}$$

where ϕ is the relative phase in polarization and d the arbitrary dimension for the time bins. From the previous project [1] the states visibility in polarization shall exceed 98% for promising results in Franson visibility because the visibility in polarization is an upper bound for the Franson visibility [25].

Chapter 3

The type-II Sagnac source

3.1 Basic working principle

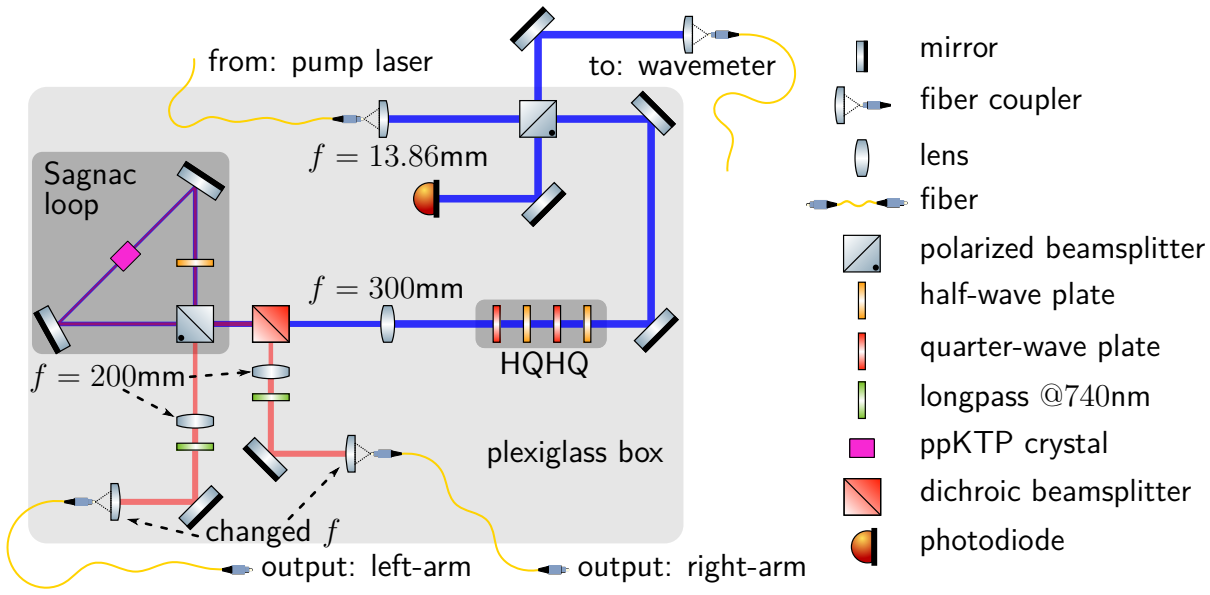

Figure 3.1: Schemata of the used type-II Sagnac photon pair source.

The type-II Sagnac source shown in Figure 3.1 can be in general grouped in four main components, the Sagnac loop itself, the focus system, the HQHQ-waveplate combination to adjust the state and the output arms to collect the state. The other parts are related to the pump beam and the alignment of the source. This includes a clean up polarized beamsplitter directly placed after the pump beam coupler. It is accomplishing three different tasks. First it splits a small part of the laser power away to analyse the wavelength of the pump laser with a wavemeter. Second it just lets pass H-polarized light with a high extinction ratio of 1:1000 to the Sagnac loop itself. Third it is used for analysing the alignment stage of the polarization Sagnac interferometer. The back reflected beam out of the polarization Sagnac interferometer should again be H-polarized light if the Sagnac loop is aligned properly. If this is not the case, the light is not interfering and comes back also as V-polarized light to the clean up polarized

beamsplitter. There it is reflected and then detected in the arm with silicon photo diode. Also a plexiglass box shown in Figure 3.2a is put on the entire setup to protect the interior from periodic changing of the outside temperatures. In order to access the HQHQ and the output arms two windows are cut in the top layer of the plexiglass box. A black cardboard plate is placed on top to cover these holes. This makes the source much better long term stable and also prevents unwanted interaction with the source in long measurement runs.
On the position marked in Figure 3.2c the maximum available pump laser power is 28.5mW when the laser is running in a stable mode and already enough power is taken away for the laser locking and the stabilisation of the Franson interferometer.

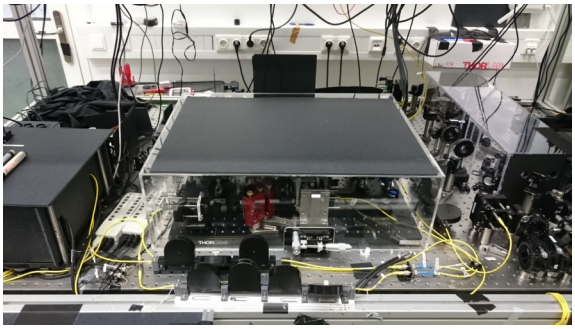

(a) Source with plexiglass box

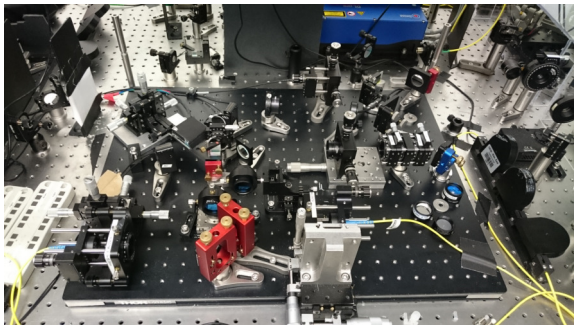

(b) Source without plexiglass box

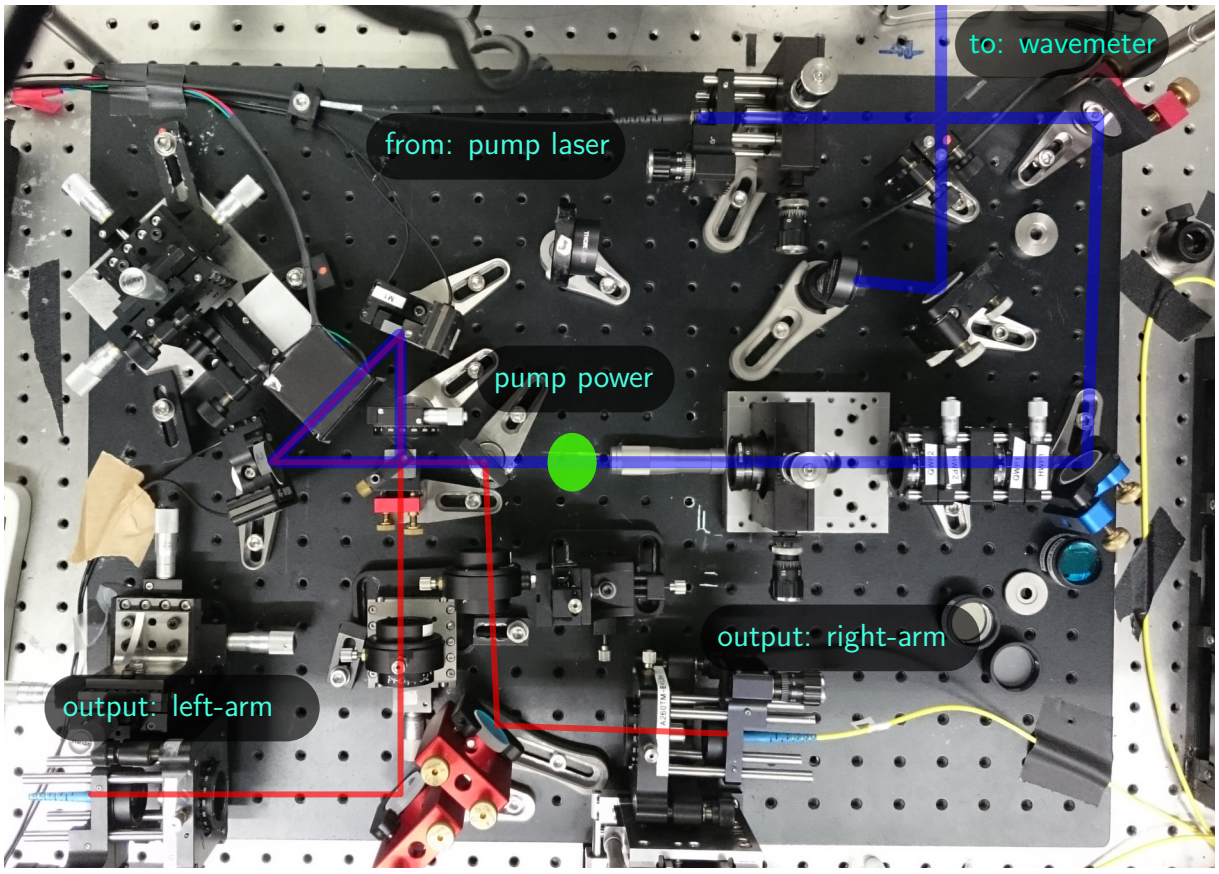

(c) Source: Top down with the position marked (green) where the pump power is measured.

Figure 3.2: Source as real setup from different points of view.

Output arms of the loop

Historically the output arms are called "signal" and "idler" where the signal arm with higher frequency and the idler arm with lower frequency. Because this source is in the chromatic degenerate case both frequencies are identical so the historical term does not make much sense in this context. Therefore the arms are just simply labeled "right" for the right arm and "left" for the left arm.
Apart from the already mentioned lenses there is a longpass $@740$nm in each arm to completely filter out the pump beam. The collimated SPDC photon modes are coupled in a fiber for further use and analysis. The lenses of those couplers are changed to optimise the brightness of the source. The dichroic beamsplitter in the begin of the rightarm shown in the schemata is in the actual technical realisation just a mirror with high transmission for UV and high reflectivity for IR.

Fixed focal parameters

In the setup are four fixed lenses. Two of them are defining the pump beam completely. Those are a C560TME-A with $f = 13.86$mm nominal focal length in the coupler and LA4579-A-ML with $f = 300$mm focusing in the center of the Sagnac loop where the ppKTP crystal is placed. The other two LBF254-200-B lenses are identical with $f = 200$mm. Both are placed in each output arm such that the focus point is also in the center of the crystal. The three lenses which are focusing into the crystal are mounted on translation stages to adjust the focus point during the alignment procedure shown in Figure 3.2.

The HQHQ

To create maximally entangled photon pairs it is necessary to adjust the pump power ratio and the relative phase in each direction of the Sagnac loop [27]. In this setup both values are directly accessible with the HQHQ which consists first out of a half-wave plate, a quarter-wave plate $@45°$, a second half-wave plate and again a quarter-wave plate $@45°$. The name HQHQ is derived from the initial letter of each plate the pump beam has to pass towards the Sagnac loop. The Jones formalism [31] is applied with arbitrarily settable angles ϕ_1 for the first half-wave plate and ϕ_2 for the second half-wave plate to a pure horizontally polarized pump beam E_{in}. The outcomes are E_H for the horizontally polarized component and E_V for the vertically polarized component.

$$E_H = -e^{-2\mathrm{i}\phi_2} \cdot \cos(2\phi_1) \cdot E_{\text{in}} \tag{3.1}$$

$$E_V = \quad e^{2\mathrm{i}\phi_2} \cdot \sin(2\phi_1) \cdot E_{\text{in}} \tag{3.2}$$

The polarized beamsplitter divides this beam into its two components. Because the extinction ratio is not identically for both arms it is necessary to adjust the power splitting. This is achieved with the first half-wave plate by comparing Equations (3.1) and (3.2). By neglecting the global phase the relative phase ϕ between both pump directions is direct proportional to $4 \cdot \phi_2$. So with the HQHQ it is possible to adjust the relative phase and the power ratio in the Sagnac loop.

Sagnac loop

The Sagnac loop is a polarized Sagnac interferometer. It consists out of a polarized beamsplitter, two mirrors, a half-wave plate and the 30mm long ppKTP crystal (see Section 1.1.4). The crystal is placed on a Peltier-element to control the temperature of the crystal with the accuracy of ± 0.1K.
The polarized beamsplitter divides the pump beam in the clockwise oriented path with H-polarized light and in the counterclockwise oriented path with V-polarized light (see fig. 3.3). The counterclockwise propagating light is passing a dual wavelength half-wave plate oriented

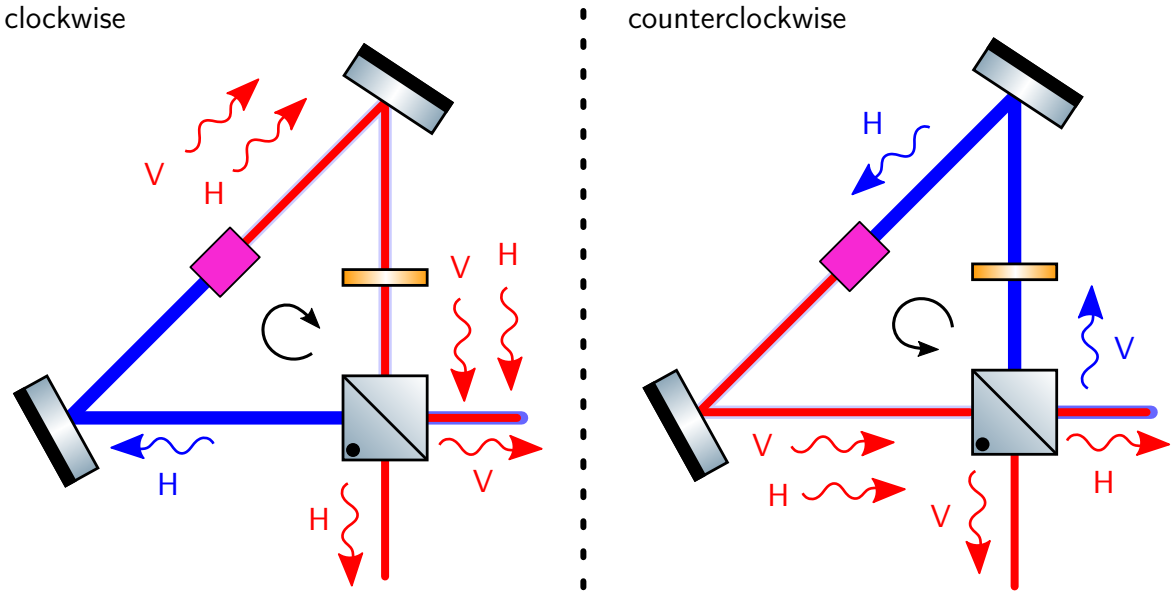

Figure 3.3: Working principle of the Sagnac loop

at $45°$ and is thereby turned form V to H polarization. In the center of the Sagnac loop is the ppKTP crystal (pink) placed. The pump beam passes the crystal from both directions with H-polarized light. So two SPDC photons could be created out of one pump photon. This photon pairs continue their propagation in the same direction as their pump photon. The clockwise propagating photon pairs have to pass the half-wave plate and flipping their polarization. Either propagation direction is returning back to the polarized beamsplitter. For the clockwise propagation beam a H-polarized photon enters the left output arm and a V-polarized photon enters the right output arm. For the counterclockwise propagation beam a V-polarized photon enters the left output arm and a H-polarized photon enters the right output arm. Through the effect of the half-wave plate the wavelength of photons in each arm is identical no matter from which propagation direction they are. Through the symmetry of the interferometric setup it is not possible to determine from which propagation direction the photons are coming. This creates the quantum mechanical state

$$|\Psi_{\text{pol}}\rangle = \left(|H\rangle_{\text{left}}\,|V\rangle_{\text{right}} + e^{i\phi}\,|V\rangle_{\text{left}}\,|H\rangle_{\text{right}}\right)/\sqrt{2} \tag{3.3}$$

where ϕ is the relative phase between H and V component of the pump beam before the polarized beamsplitter [27].
The half-wave plate provides also the additional effect to make the photons not just indistin-

guishable in wavelength but also in the time domain because different propagation velocities inside the crystal and so time delays are compensated. This is caused by the effect that the photons end up with different delays in each output arm but these time delays are equal for both polarizations in each arm and thereby independent from their propagation direction [3].

3.1.1 Spectrum

The source shall be wavelength degenerate. This means the photons in both output arms have all the same wavelength. Therefore it is important to know the dependency between the temperature of the crystal and the wavelength of the emitted photons in each arm. A single photon spectrometer with a maximal accuracy of 1.7nm FWHM is used to measure the mean wavelength of the photons in each arm separately for different crystal temperatures. The mean wavelength and the FWHM is obtained for each measurement of the spectral density by applying a Voigt function (convolution of Gaussian and Lorentz function) fit (see fig. 3.5). The values are gauged with the known pump wavelength of the stabilized potassium hyper fine structure line $\lambda_p = 404.414$nm [32, 33] while 2.006nm were subtracted from each mean value by taking care of the different refraction indices in air [34] because of energy conservation $\lambda_{\text{SPDC}} = 2 \cdot \lambda_p \cdot n_p / n_{\text{SPDC}} = 808.834$nm. Results are shown in Figure 3.4. A linear dependency

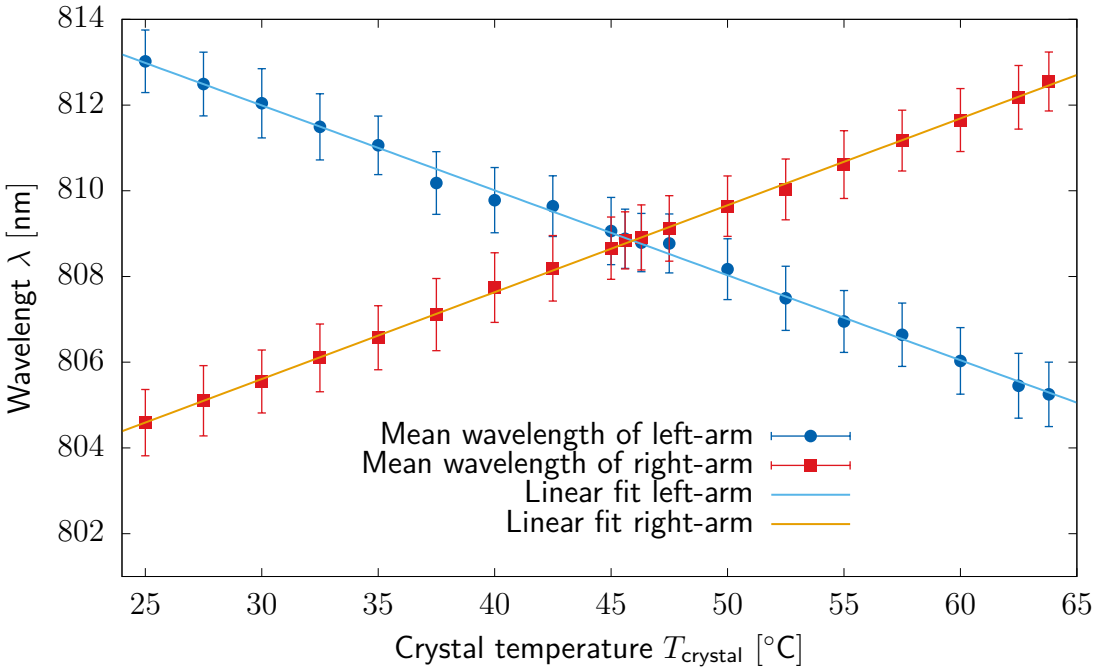

Figure 3.4: Mean wavelength λ for both output arms of the ppKTP crystal's spectral density at different crystal temperatures T_{crystal} obtained with Voigt fits. The minimal resolution of the measurement devices is 1.7nm FWHM.

can be observed for the wavelengths of the produced SPDC photons. Therefore a linear least square fit is applied to both curves. The gradient of fits matches in the ranges of their errors which is expected because of energy conservation and the absolute average is calculated.

$$\left| \frac{\lambda_{\text{SPDC}}}{T_{\text{crystal}}} \right| = (0.2027 \pm 0.0011) \frac{\text{nm}}{\text{K}} \tag{3.4}$$

The same result for KTP has been obtained by Steinlechner[4] with also ~ 0.2nm/K. The obtained FWHM with all around ~ 1.6nm are indicating that the FWHM should be smaller than measured and just limited by the maximum accuracy of the used measurement devices. Steinlechner gives for his used crystal a value of ~ 0.3nm which is a much more typical value of narrow pumped type-II ppKTP crystals.
The source shall produce photons with the same wavelength in each arm. Therefore the crystal's temperature is adjusted to $T^{\text{deg.}}_{\text{crystal}} = 45.6°\text{C}$. The degenerate case can be seen in Figure 3.5. Both spectral densities lie on top of each other with the mean at $\lambda_{\text{SPDC,left}} =$

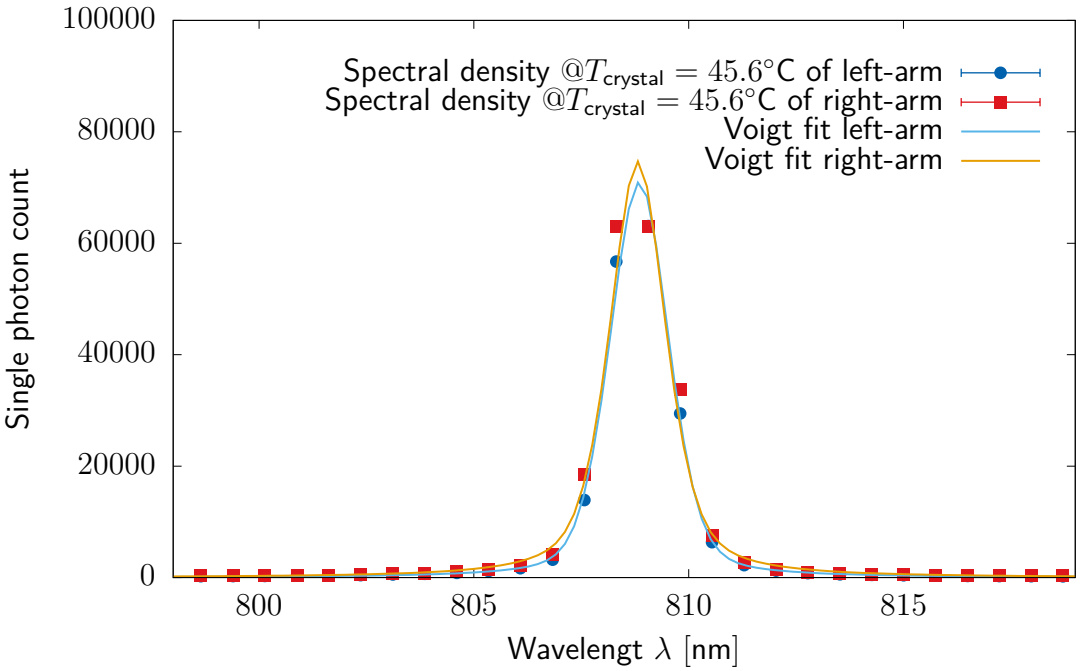

Figure 3.5: Spectral density for both output arms of the ppKTP crystal at the degenerate temperature $T^{\text{deg.}}_{\text{crystal}} = 45.6°\text{C}$

(808.84 ± 0.67)nm and $\lambda_{\text{SPDC,right}} = (808.83 \pm 0.67)$nm. The difference is 0.014nm. This is the closest option to the degenerate case with temperature steps of just 0.1K possible.

3.2 Characteristica

Sources have typical characteristics which differ also for different used focus parameters in the collimator. In order to determine them different characteristic values can be calculated out of the directly observed values. For each existing mode i the count of single clicks in certain time period R_i is measured. For two existing modes i and j the photon pairs count rate $R_{\text{CC},i,j}$ can be determined by a defined coincidence window t_{CoW} where in both modes a click appears - a so called coincidence - in the time frame. By applying half-wave plates and polarized beamsplitters different additional polarization dependent modes can be created. Those are referring then to the different polarization to fully determine the quantum behavior of a source.

Brightness

The Brightness B_i is a count rate R_i normalised by the laser power P. It is a scale for how effective the pumped laser power in the Sagnac-loop is used.

$$B_i = \frac{R_i}{P} \tag{3.5}$$

The source itself has two output modes (left, right). Thus the average count rate

$$R_{\text{Avg}} = \frac{1}{2} \cdot (R_{\text{left}} + R_{\text{right}}) \tag{3.6}$$

for singles is defined. With the count rates defined for the photon pairs of both output modes R_{CC} and average singles R_{Avg} the brightness B_{CC} and B_{Avg} can be calculated by Equation (3.5).

Heralding

The Heralding η_i is defined by ratio between singles and photon pairs count rate. It is a scale how effective the photons are coupled into the single mode fiber because the photons are created in pairs. To determine transmission losses and the efficiency of the detectors properties in the whole setup of one output mode

$$\eta_i = \frac{R_{\text{CC},i,j}}{R_i} \tag{3.7}$$

is used. With the transmission loss τ_i and the detector efficiency η_i^D and the ith mode the real heralding $\tilde{\eta}_i$ can be calculated

$$\tilde{\eta}_i = \frac{\eta_i}{\tau_i \eta_i^D} \tag{3.8}$$

This should be kept in mind because just the directly observed values η_i are being used. The reason for it is that the same detectors and fibers are used for the overarching experiment this source was build for. There are just additional fibers and optics involved which lower additionally the transmission and thus the heralding because there will appear an additional τ into the term of Equation (3.8). In order to better characterise the source itself an average heralding over both output modes is sufficient:

$$\eta_{\text{Avg}} = \frac{R_{\text{CC,left,right}}}{\sqrt{R_{\text{left}} \cdot R_{\text{right}}}} \tag{3.9}$$

The heralding values are just the directly observed values for the entire setup where no corrections are applied to calculate just the real heralding of the source itself.

Visibility

The source produces the state

$$|\Psi\rangle = \frac{1}{\sqrt{2}}\left(|H\rangle|V\rangle + e^{\mathrm{i}\phi}|V\rangle|H\rangle\right) \tag{3.10}$$
$$= \frac{1}{2\sqrt{2}}\left[\left(1+e^{\mathrm{i}\phi}\right)(|D\rangle|D\rangle - |A\rangle|A\rangle) + \left(1-e^{\mathrm{i}\phi}\right)(|D\rangle|A\rangle - |A\rangle|D\rangle)\right]$$

where ϕ can be set individually. This shall be a maximally entangled state so $\phi \to \pi$.

$$|\Psi^-\rangle = \frac{1}{\sqrt{2}}(|H\rangle|V\rangle - |V\rangle|H\rangle) = \frac{1}{\sqrt{2}}(|D\rangle|A\rangle - |A\rangle|D\rangle) \tag{3.11}$$

Alternative can $\phi \to 0$

$$|\Psi^+\rangle = \frac{1}{\sqrt{2}}(|H\rangle|V\rangle + |V\rangle|H\rangle) = \frac{1}{\sqrt{2}}(|D\rangle|D\rangle - |A\rangle|A\rangle) \tag{3.12}$$

$|\Psi^+\rangle$ and $|\Psi^-\rangle$ are two of the four Bell states. Preferable is the basis independent state $|\Psi^-\rangle$ which retains its mathematical structure in all bases. So for the $|\Psi^-\rangle$ are the orthogonal polarization pairs for each arm from interest while the equal polarization pairs are considered to be unwanted. So the Visibility

$$V(i\,j, i'j') = \frac{R_{\mathrm{CC},i,j'} + R_{\mathrm{CC},j,i'} - (R_{\mathrm{CC},i,i'} + R_{\mathrm{CC},j,j'})}{R_{\mathrm{CC},i,j'} + R_{\mathrm{CC},j,i'} + R_{\mathrm{CC},i,i'} + R_{\mathrm{CC},j,j'}} \tag{3.13}$$

is defined out of 4 different photon pair count rates in polarization filtered modes ($i \perp j$ and $i' \perp j'$). The first index of the count rates is referred to the left-arm and its content is the actual observed basis. The second index of the count rates is analog the measurement basis of the right-arm. For equal bases in both arms $i = i'$ and $j = j'$ are equal and so for the $V(i\,j, i\,j)$ the short notation $V_{i\,j}$ is introduced. This results in the two visibilities V_{HV} and V_{DA} for the two measurement bases HV and DA.
The HV-visibility is considered to be good $V_{\mathrm{HV}} \approx 100\%$ because the here used setup is creating in the HV-basis. The DA-visibility shall be as high as possible. Alternatively the DA-visibility can chosen to be negative. This refers to the $|\Psi^+\rangle$ state which can be a practical alternative for some different experiments. To set the two different states the DA-visibility has to be maximized for the $|\Psi^-\rangle$-state and minimized for the $|\Psi^+\rangle$-state according to the definition in Equation (3.13).

3.3 Problems of brightness optimised sources

The main advantage of type-0 sources is that they are much brighter than type-II sources by the order of two to three magnitudes for similar setups (see present overview [35]). The type-0 has just one output mode and to couple into just one spatial mode is so much easier. The

spectral bandwidth of the created photons is one magnitude smaller for the type-II source. Also the change of the center wavelength depending on the crystal temperature is with a magnitude of one lower than for type-0 [4]. The type-II source has directly two different spatial output modes in comparison to the type-0 source. The type-0 source uses typically a chromatic depending splitting to generate two separate spatial modes. Apart from the brightness a type-II source has three major advantages in comparison to the type-0 source.
These previously described advantages of the type-II source are much more important when keeping in mind that after the free-space link a narrow band filter is installed to filter out unwanted stray light from the environment caused by the sun. These filters are super narrow and so highly sensitive to changes in the center wavelength. A small bandwidth is necessary to reduce the environmental photons as good as possible and therefore the small bandwidth of the produced photons is necessary. This is the reason why just a type-II source is a good choice for this experiment.

Calculating focus parameters for a high brightness is not a straight forward task because many authors claiming different dependencies how the brightness of a source can be determined and increased. The definitions and relations between the different notations of contributing authors are explained in Section 3.3.1.
Ling et al.[36] claim that the beam waists of the SPDC photons w_{SPDC} and the pump beam w_p should satisfy the equation $\sqrt{2}w_p = w_{\text{SPDC}}$. Instead Kurtsiefer et al.[37] proposing $w_p = w_{\text{SPDC}}$ as the best choice. Ljunggren and Tengner[38] are claiming an ideal brightness in between those to previous suggestions with their ideal relation between $\xi_p \approx 0.5$ to 1.0 and $\xi_{\text{SPDC}} \approx 1.0$ to 1.5. They are additionally claiming that the photon pair rate increases with $\propto \sqrt{L}$ of the length of the crystal L. Bennink[2] contradicts this theory with the proposition that the photon pair rate is independent from the crystal. For just brightness he suggest $\xi_p = \xi_{\text{SPDC}}$ and he also suggests an equation for high spectral brightness to fulfill: $\xi_{\text{SPDC}} \approx \sqrt{2.84\xi_p}$. To fulfill both equations $\xi_p \approx \xi_{\text{SPDC}} \approx 1$. All authors agree that the best results can be found for a focus parameter for the source around $\xi_p \approx 1 \pm 0.5$.

3.3.1 Theoretical values

To find the theoretical values for good focus parameter the paper of Bennink[2] is used. He calculated for his approximation the quantum mechanical SPDC process in combination with collinear Gaussian beams optics. His theoretical results fit well with the experimental results of Steinlechner[4]. Bennink's final result is that the focal parameter ξ for pump and collector beams have just to be scaled equally for the length of the crystal $L = 30$mm and the beam waist w_j which are directly related to the used focal lengths f.

$$\xi_j = \frac{L\lambda_j}{2\pi n_j w_j^2} \tag{3.14}$$

λ_j is the wavelength, j can be the pump mode or the SPDC-photon modes and n_j is the refractive index of the crystal for the different wavelengths. The average of the refractive indices from the different polarizations inside the crystal are used with $n_{\text{SPDC}} = 1.824$.
The theory predicts that the highest pair collection probability for a source can be achieved for $\xi > 10$. In comparison to Fedrizzi[3], he observed the highest brightness for values $\xi_p \approx 1.4$ for

a 25mm long crystal. Using this and Bennink's formula for wavelength's narrow band optimal parameters $\xi_{\text{SPDC}} \approx \sqrt{2.84\xi_p}$. To find lenses which fulfill these conditions Equation (1.4) is used to obtain a good approximation for the beam waist inside the ppKTP-crystal.

$$w_j \approx \frac{f_{\text{loop},j}}{2 \cdot f_{\text{coupler},j}} \text{ø}_{\text{fiber},j} \tag{3.15}$$

This approximation holds well even with a distance between the lenses, where the beam is collimated, of less than 0.5m and the refractive index $1 < n < 2$ of the crystal compared with an exact calculation of Gaussian beam optics with matrix optics. The relative error is less than 0.2% for the used wavelength. This calculation gives just the extra hint that the focus lens inside the crystal has to be moved further away from the Sagnac loop. For the case of the pump beam this is ~ 4mm.
With the known fiber mode field diameter $\text{ø}_{\text{fiber},p} = 2.5\mu$m for the pump fiber and $\text{ø}_{\text{fiber,SPDC}} = 5.0\mu$m according to the manufacturer. $f_{\text{loop},j}$ is the focal length of the fixed lens which is focusing into the Sagnac loop and $f_{\text{coupler},j}$ is the focal length of the fiber coupler lens. Combining Equations (3.14) and (3.15) to obtain the relation r_j of the focal lengths depending on the chosen ξ_j.

$$r_j = \frac{f_{\text{loop},j}}{f_{\text{coupler},j}} = \sqrt{\frac{2 \cdot L \cdot \lambda_j}{\pi \cdot n_j \cdot \xi_j \cdot \text{ø}^2_{\text{fiber},j}}} \tag{3.16}$$

For the pump beam this gives us $r_p = 20.726$. The already presented lenses in section 3.1 with $f_{\text{coupler},p} = 13.86$mm and $f_{\text{loop},p} = 300$mm fulfill this condition with $r_p = 21.645$. Combined with those lenses the focal parameter is $\xi_p = 1.383$. Using this to determine $\xi_{\text{SPDC}} = 1.982$ and $r_{\text{SPDC}} = 13.013$. A lens pair which fulfill this relation is $f_{\text{coupler,SPDC}} = 15.29$mm and $f_{\text{loop,SPDC}} = 200$mm with $r_{\text{SPDC}} = 13.080$. This is close to the wanted parameters and by using different coupler lenses it is still possible to vary the ξ_{SPDC} by exchanging the coupler lenses.
By the attempt to increase the visibility the pump fiber was changed (see section 3.3.2) and so also the focus parameter for the source. The fiber was replaced with the only other available fiber for high UV-power throughput but the fiber has a different mode field diameter. With a mode field diameter $\text{ø}_{\text{fiber},p} = 4.2\mu$m the focus parameter of the pump is just $\xi_p = 0.489$ which is way lower than originally planned. But the change of the focus parameter solved the problem with the visibility so the changed parameters were kept for a good visibility for a minimal cost in brightness of $\sim 5\%$. Again using Bennink's formula for wavelength's narrow band optimal parameters $\xi_{\text{SPDC}} \approx \sqrt{2,84\xi_p} = 1.178$. The new $r_{\text{SPDC}} = 16.875$ which is still in the same regime for the focus parameter of the coupler. The best results for the narrow band are expected to be $f_{\text{coupler,SPDC}} = 11.85$mm if $f_{\text{loop,SPDC}}$ stays the same. The brightest value are expected for the single photon rate at $f_{\text{coupler,SPDC}} \approx 17.5$mm and for the photon pair rate at $f_{\text{coupler,SPDC}} \approx 13.0$mm. So the existing lens $f_{\text{coupler,SPDC}} = 15.29$mm in between those focal length is the one from the theoretical point of view expected best lens for the brightness if the other three focal lengths stay fixed.
To determine the focal parameter ξ_{SPDC} for a $f_{\text{coupler,SPDC}}$ with the fixed focal length $f_{\text{loop,SPDC}}$

a combination of Equations (3.14) and (3.15) gives:

$$\xi_{\mathsf{SPDC}} \approx \frac{2 \cdot L \cdot \lambda_{\mathsf{SPDC}}}{\pi \cdot n_{\mathsf{SPDC}}} \left(\frac{f_{\mathsf{coupler,SPDC}}}{f_{\mathsf{loop,SPDC}} \cdot \text{Ø}_{\mathsf{fiber,SPDC}}} \right)^2 \approx f^2_{\mathsf{coupler,SPDC}} \cdot \frac{8479.1}{\mathsf{m}^2} \tag{3.17}$$

Fit functions

By evaluating the formulas of Bennink (see appendix B) possible functions for fitting the brightness results of the single photons and photon pair rate can be obtained, as well as a function for the heralding. Using Bennink functions and replacing the ξ_{SPDC} with Equation (3.17) and applying all other values with the parameters known while a small variation of the beamwaist of the SPDC photon ($C1 = 1$) and the pump beam ($C2 = 1$) were allowed. For the single photon brightness

$$B_{\mathsf{Avg}}(f) \approx N_{\mathsf{Avg}} \left(\frac{5.96 \cdot \tan^{-1}\left(\frac{7.51 \cdot f^2 \sqrt{\frac{8.40 \cdot 10^{-12} \cdot C1^2}{C2^2 \cdot f^2} + 2.90 \cdot 10^{-13}}}{C1^2 \sqrt{\frac{2.07 \cdot 10^{-9} \cdot C2^2 \cdot f^2}{C1^2} + 2.5 \cdot 10^{-7}}} \right)}{\sqrt{\frac{8.40 \cdot 10^{-12} \cdot C1^2}{C2^2 \cdot f^2} + 2.90 \cdot 10^{-13}} \sqrt{\frac{2.066 \cdot 10^{-9} C2^2 \cdot f^2}{C1^2} + 2.5 \cdot 10^{-7}}} + \frac{5.55 \cdot \tan^{-1}\left(\frac{8.06 \cdot f^2 \sqrt{\frac{7.29 \cdot 10^{-12} \cdot C1^2}{C2^2 \cdot f^2} + 2.90 \cdot 10^{-13}}}{C1^2 \sqrt{\frac{2.07 \cdot 10^{-9} \cdot C2^2 \cdot f^2}{C1^2} + 2.5 \cdot 10^{-7}}} \right)}{\sqrt{\frac{7.29 \cdot 10^{-12} \cdot C1^2}{C2^2 \cdot f^2} + 2.90 \cdot 10^{-13}} \sqrt{\frac{2.07 \cdot 10^{-9} C2^2 \cdot f^2}{C1^2} + 2.5 \cdot 10^{-7}}} \right) \tag{3.18}$$

and for the photon pair brightness

$$B_{\mathsf{CC}}(f) \approx N_{\mathsf{CC}} \frac{1.49 \cdot C1^2 \cdot C2^2 \cdot f^2 \cdot \tan^{-1}\left(\frac{7.93 \cdot 10^{-3} \cdot C1^2 \cdot f^2 + 1.46 \cdot 10^{-4} \cdot C2^2 \cdot f^4}{C1^4 + 1.65 \cdot 10^{-2} \cdot C1^2 \cdot C2^2 \cdot f^2} \right)}{C1^4 + 3.499 \cdot 10^{-2} \cdot C1^2 \cdot C2^2 \cdot f^2 + 3.05 \cdot 10^{-4} \cdot C2^4 \cdot f^4} \tag{3.19}$$

and for the heralding

$$\eta_{\mathsf{Avg}}(f) = N_\eta \cdot \frac{B_{\mathsf{Avg}}(f)}{B_{\mathsf{CC}}(f)} \tag{3.20}$$

numerical functions can be obtained for $f[\mathsf{mm}]$ and the normalisation constants N_{Avg}, N_{CC} and N_η. The photons of the left-arm and right-arm are equal in the theory so $R_{\mathsf{left}} = R_{\mathsf{right}} = \sqrt{R_{\mathsf{left}} \cdot R_{\mathsf{right}}} = 0.5 \cdot (R_{\mathsf{left}} + R_{\mathsf{right}})$ and the result from the theory is obtained. The variation parameters $C1$ and $C2$ are equal for all three least square fits applied to the brightnesses and the heralding in Section 4.2.

3.3.2 Initial problem with the visibility

After changing the focus parameters with the original planned ones the source had a severe problem with the visibility in the DA-basis. With a starting point at $V_{\mathsf{DA}} \approx 84\%$ and a strange

temperature dependency of the loop shown in Figure 3.6. The attempt was made to protect

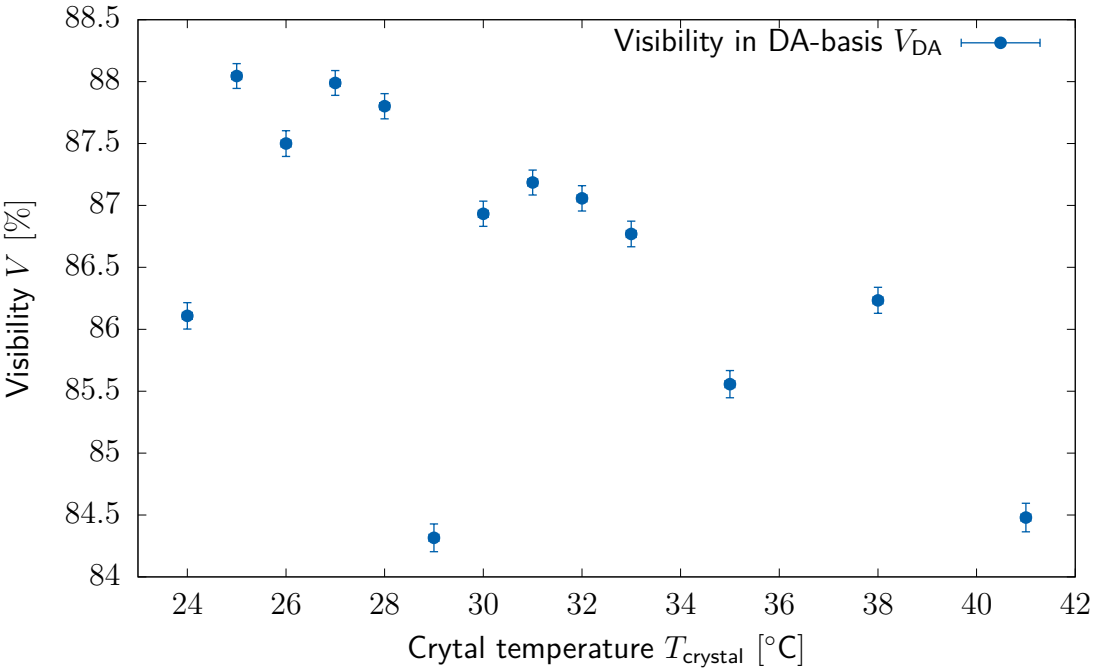

Figure 3.6: Visibility in DA-basis measured for optimal set up in the degenerate case with just $V_{\mathrm{DA}} \approx 84\%$ for different crystal temperatures T_{crystal}.

the crystal better from the environment to avoid temperature gradients from the bottom side where the oven was placed to the top side which was exposed to the air at room temperature. This idea did not improve much. It is not possible to reduce the temperature because the used narrow band filters were bought explicitly for the degenerate case. So many different attempts were made to increase the visibility.
The next try was to correct the geometry of the loop to reach a perfect right-angled isosceles triangle. In combination with many iteration steps (see section 4.1.3) in the forwarding process the DA-visibility could be increased up to $V_{\mathrm{DA}} \approx 94\%$ in the degenerate case. The classical visibility of the Sagnac interferometer was measured with an installed photodiode in the destructive arm of the polarized beamsplitter with $1 : 200$. The next attempt was to exchange the small $1/4''$ mirrors inside the Sagnac loop with $1''$ mirrors. This increased the visibility just slightly to $V_{\mathrm{DA}} \approx 95\%$.
This brought the idea up that the pump beam could be cropped by the extension of the pump beam diameter in comparison to the previous used beam. Therefore the small diameter ($1/2''$) quarter- and half-wave plates of the HQHQ were exchanged with their bigger diameter version of $1''$. This did not change anything in the DA-visibility with still $V_{\mathrm{DA}} \approx 95\%$. But nevertheless the decision was made to use a beam expander and a shorter focal lens after the pump laser's fiber because the pump beam could be also cropped here. These were adjusted in such a way that the beam diameter again become $\varnothing_{\mathrm{coll}} = 2.86$mm for the collimated beam after the pump laser coupler and the beam expander as before with not exchanged lenses for the pump laser's fiber coupler. This did not help anything in terms of the DA-visibility.
The beam profile after the coupler was not looking pretty circular shaped. While analysing the beam which was shining into the fiber on the other side a horrible beam shape was obtained (see fig. 3.7a). Therefore the fiber was removed and replaced with a spatial filter built out of a pinhole because the used fiber was not built for such higher power throughput and

the loss with 70% was untypical high. The beam was direct deflected with the help of two mirrors into the source and the beam diameter was adjusted with the beam expander to the favoured diameter. This increased the DA-visibility up to $V_{\text{DA}} \approx 97.5\%$ but the spatial filter reduced the power by 75%. A special fiber for high power resistance for UV-light was used. This fiber served also as a very good spatial filter and the power through put is with just 60% loss much better. Thereby the spatial filter and the beam expander are removed while the visibility was still $V_{\text{DA}} \approx 97.5\%$ with the original planned lens in the pump laser's fiber coupler. A newer version of this special fiber was obtained with the hope to get more power through but this was actually not the case. The result of the spatial filter can be seen in

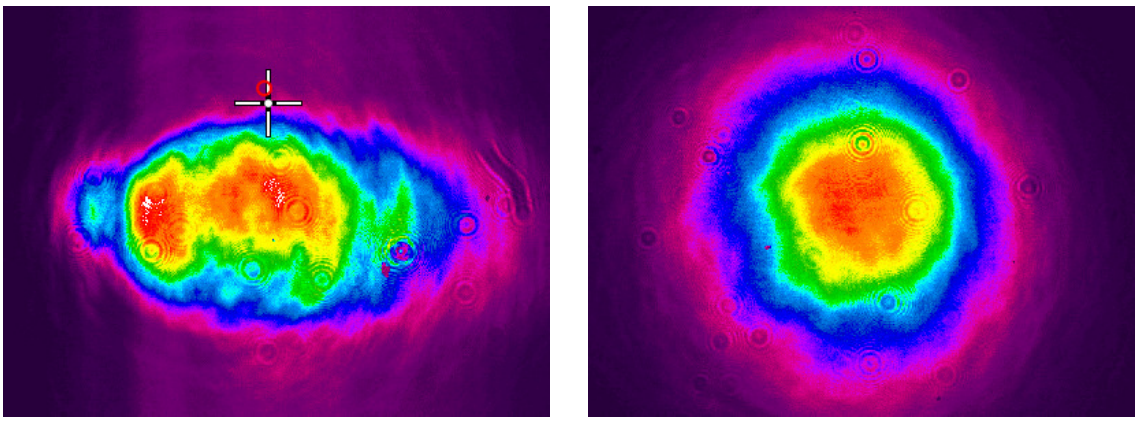

(a) before (b) after

Figure 3.7: Spatial filtering of the pump laser beam captured by a Spiricon beam profiler. The color scale is temperature weighted where warmer colour means more intensity.

Figure 3.7. A higher count rate through more available power and also a better visibility in DA with $V_{\text{DA}} \approx 98\%$ was obtained. By checking the beam diameter of the collimated pump beam in Figure 3.7b $\text{ø}_{\text{coll}} = 1.70$mm was obtained. By using Equation (1.4) and the known wavelength $\lambda_p = 404.414$nm and focal length $f = 13.86$mm the mean field diameter of the fiber has to be $\text{ø}_{\text{fiber}} = 4.20\mu$m. This value fits exactly with another fiber offered from the manufacturer but the actual label on it shows a different specification - the same as before. Nevertheless this wrong labeled fiber could produce from the theoretical point of view also good results with the different focus parameter and the already better measured results led to the decision to stay with these focus parameter for the pump laser.
After all the exchanges of the used parts the focus lens towards the Sagnac loop was slightly tilted. Correcting this small issue provides the wanted high visibility in DA with $V_{\text{DA}} \approx 99\%$.

Chapter 4

Different focus parameters

4.1 Measurement

In order to fully characterize the source with different coupler lenses the properties in section 3.2 are measured for each lens. With the results for brightness, heralding and visibility it is possible to determine the lens which fits best for the noiseresilient free-space high dimensional non-local interference experiment. First a high visibility of over 98% is wanted, second a high brightness of single photons with a certain limit and finally corresponding to that limit the highest heralding.

4.1.1 Devices

The pump laser power is measured between the dichroic beamsplitter and the pump focus lens $f = 300$mm in Figure 3.2c because this position is easy accessible from outside through the hole in the top plane of the plexiglass box. A Si-photodiode is placed in this position before every brightness measurement and the pump power is adjusted exactly at $P = 1.000$mW. The photodiode has a measurement uncertainty of $\pm 5\%$ according to the manufacturer and is the source of the biggest uncertainty in the brightness measurement.

The different orthogonal polarizations in one output mode of the source are measured simultaneously by the polarization analysing module shown in Figure 4.1. The Wollaston prism works like a polarized beamsplitter with the difference that the spatial outputs are parallel with a small spatial offset. The H-photons are going straight through the prism while the V-photons are getting a small offset. This offset is used to reflect each of the spatial separate output modes into a separate coupler. The coupler's fibers to the detectors are multi mode fibers because there is no need anymore to maintain the polarization and the coupling efficiency of a multi mode fiber is much higher than those of a single mode fiber. To avoid unwanted stray light be coupled into the multi mode fiber the whole setup is placed in a black box (see fig. 4.2). With the half-wave plate in front of the Wollaston prism it is possible to rotate the linear polarization in any needed basis. By choosing the measurement basis of both input modes to be in the same basis the visibility can be determined either in HV or in DA. To calculate the visibility by Equation (3.13) the four photon pair count rates $(R_{\mathrm{CC,H,V}}, R_{\mathrm{CC,H,H}}, R_{\mathrm{CC,V,H}}, R_{\mathrm{CC,V,V}})$ for HV-basis V_{HV} and $(R_{\mathrm{CC,D,A}}, R_{\mathrm{CC,D,D}}, R_{\mathrm{CC,A,D}}, R_{\mathrm{CC,A,A}})$

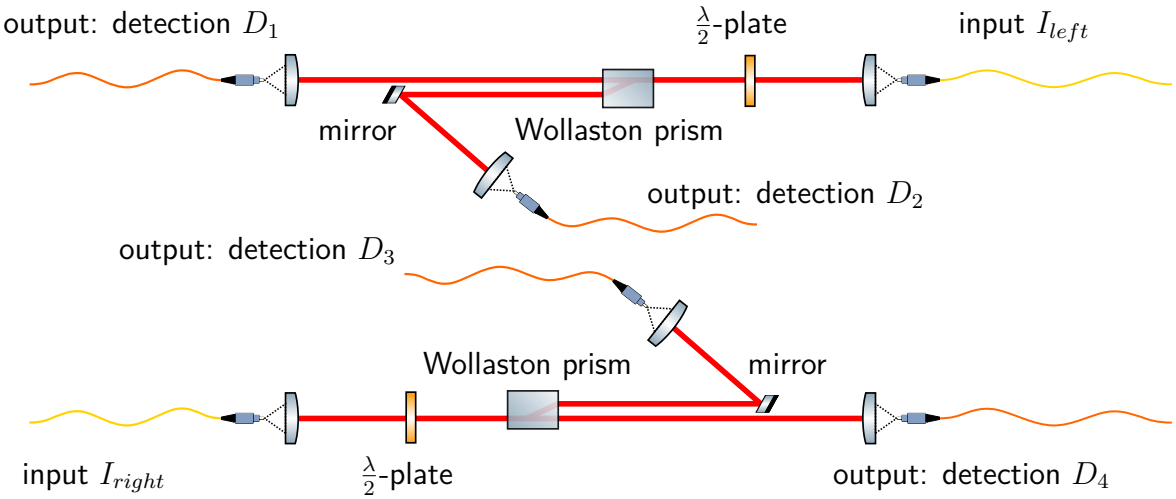

Figure 4.1: The polarization analysing module splits an input mode in two modes where the polarization between those two modes is orthogonal. This module consists out of two input modes. For each input mode the polarization basis can be chosen individually by the half-wave plate.

for DA-basis V_{DA} are necessary. In HV-basis this count rates are obtained by setting both half-wave plates to $0°$ corresponding to their fast axis. Then detector D_1 is measuring the H-photons of the left-arm and detector D_2 is measuring the V-photons of the left-arm. Detector D_3 is measuring the V-photons of the right-arm and detector D_4 is measuring the H-photons from the right-arm. By finding the photon pairs between the polarization dependent count rates R_{CC} of the left-arm and right-arm are observed. These are for D_1 and D_3 the photon pair count rates $R_{\mathrm{CC,H,V}}$, for D_1 and D_4 the photon pair count rate $R_{\mathrm{CC,H,H}}$, for D_2 and D_4 the photon pair count rate $R_{\mathrm{CC,V,H}}$ and for D_2 and D_3 the photon pair count rate $R_{\mathrm{CC,V,V}}$. To measure the DA-basis the half-wave plate is set to $22.5°$. This rotates the incoming D-polarization to H-polarization and the A-polarization to V-polarization. So the polarization analysing module can measure the DA-visibility analogously to the HV-visibility.

The detectors used for detecting the single photon in the end are Excelitas SPCM-800-11-FC. These are special silicon avalanche photo diodes for efficiently counting single photons which are emitting a TTL signal digitized by a Swabian Time Tagger. The detectors have an efficiency of 66% to detect an arriving photon according to the manufacturer. Because a high precision time-bin resolution is necessary the non-linearity of the detectors should be as small as possible. The limit is defined with a maximal accepted deviation of 5%. This corresponds to $\sim 1.75 \cdot 10^6/\mathrm{s}$ detected counts. By using the maximal available pump power $P_{\mathrm{max}} = 28.5\mathrm{mW}$ a single photon brightness cap can be obtained with

$$245 \cdot \frac{10^3}{\mathrm{mW} \cdot \mathrm{s}} \tag{4.1}$$

to not exceed the cap of the detectors for non-linear behaviour. The digitized photon counts are basically just timestamps. To find coincidences two timestamps have to match in a certain

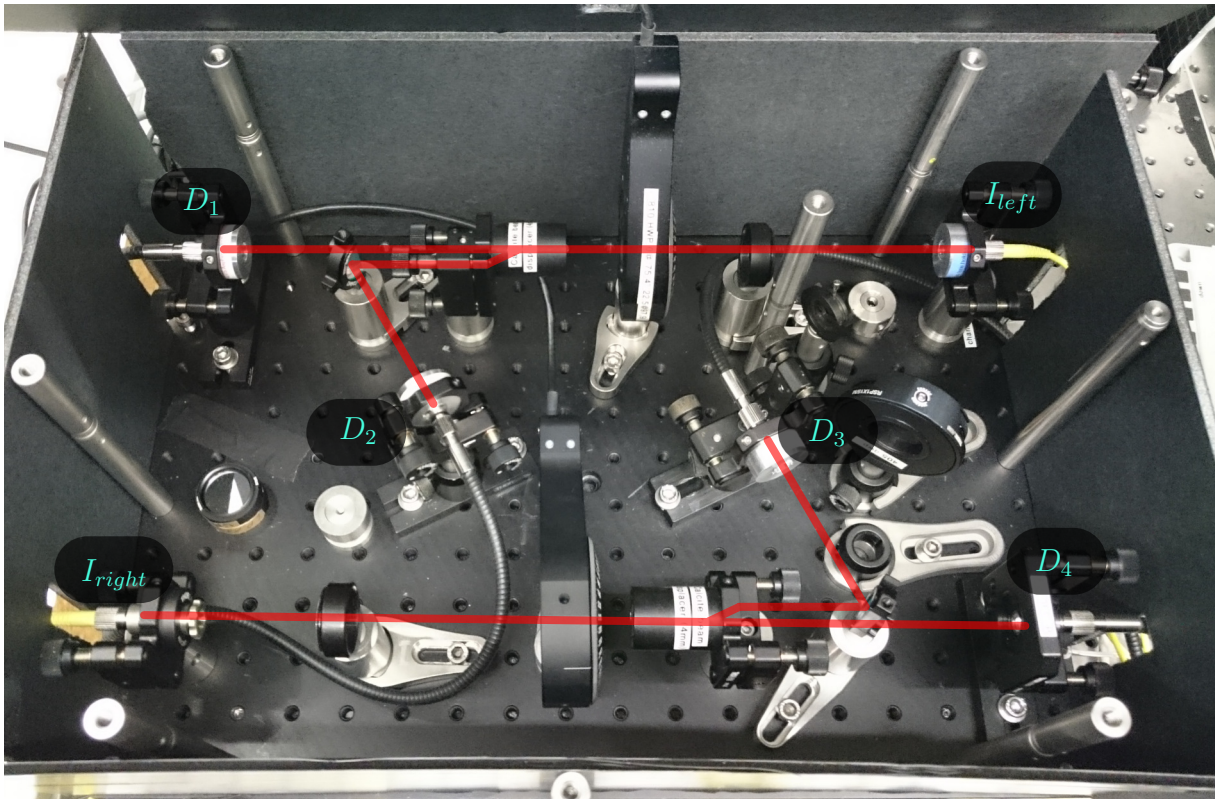

Figure 4.2: The polarization analysing module shown in Figure 4.1 as real setup.

time window - the coincidence window. But through different fiber and cable lengths for the different channels the length differs and so also the time differences need to be corrected. Therefore an individual offset has to be found for each channel to maximize the coincidences. These offsets are digitally applied in the evaluation algorithm of the software [23].

4.1.2 Lenses

For optimising the brightness while keeping a high visibility different coupler lenses are used (see Table 4.1). The perfection of the focal lengths are 1% according to the manufacturers'

Name	f_{label}[mm]	f_{chrom}[mm]	ξ_{SPDC}
352110V810-99-MT	6.24	6.25	0.3312
A375TM-B	7.50	7.49	0.4757
C060TMD-B	9.6	9.67	0.7929
C220TME-B	11.00	11.08	1.0409
C560TME-B	13.86	13.97	1.6547
C260TME-B	15.29	15.31	1.9875
C280TM-B	18.40	18.42	2.7756

Table 4.1: Different used coupler lenses. f_{label} is the focal length written on their label. f_{chrom} is the focal length after applying the chromatic correction for each lens to 810nm. Focal parameters ξ_{SPDC} are calculated with Equation (3.17).

data sheet. The chromatic aberration is also calculated by the manufacturers' data sheet. For

longer focal length the single mode fiber has a bigger visible cross sectional area. Therefore it is expected to see more photons for longer focal length. The question now related to the lenses is: When will the visibility start to drop? The photons in the outer visible area of the cross section of the beam waist have stronger tilted $\mathbf{k}$-vectors. This is why the optics start to act as measuring devices and the state collapses before the photons can be coupled into the fiber. This is caused by the reason that the second lens is fixed and therefore just a bigger cross sectional area of this lens shining into the fiber.
The second question regards the heralding: Does it stay constant for higher focal length or does it drop because the coupler lenses see the down converted photons through the best form SPDC focus lenses? These lenses are just perfect at their center but for transmission points further away from the center the quality of the collimation decreases slightly. So it could be possible that for higher focal lengths the photon pair count rate does not increase significantly anymore.

4.1.3 Alignment

To align the source from scratch the alignment procedure is shown in Figure 4.3. It begins with collimating the pump beam (see fig. 4.3a). The pump beam is filtered by a polarized beamsplitter to get a clean H-polarized beam. The minor parts which are reflected are used for the wavemeter to monitor the wavelength. The H-polarized beam is reflected twice by two mirrors. The beam passes the already installed dichroic beamsplitter and passes through the dual wavelength polarized beamsplitter which is the starting point for the Sagnac loop. The Sagnac loop is set up in a isosceles right triangle and the half-wave plate (HWP) is adjusted to be $45°$. The beam is then reflected and passes back to the cleaner polarized beamsplitter. By tilting the mirrors in the loop the incoming and outgoing beam to the Sagnac loop shall perfectly overlap. If this is the case, the pump beam can be used to adjust the two output arms and roughly couple the beam into the single mode fibers in both arms shown in Figure 4.3b. For the left-arm the half-wave plate inside the loop should be $0°$. For the right-arm the half-wave plate inside the loop should be $45°$ where the beam just weakly exists after dichoric beamsplitter. The half-wave plate stays at $45°$ for Figure 4.3c. To accomplish this the unwanted output port of the half-wave plate is minimized. The HQHQ is inserted afterwards and on the fourth until now not used output is placed a mirror, a lens and a screen to observe the interference pattern. This interference pattern is created by turning the first half-wave plate of the HQHQ (marked with an arrow) to $22.5°$ so the H-polarization becomes D-polarization and the Sagnac loop with the polarized beamsplitter can act as an interferometer. The observed interference pattern should be totally destructive in the ideal alignment point of the Sagnac loop. This is used to create now perfectly destructive interference with the two mirrors inside the loop. Thereby it is important to check that the beams are still overlapping otherwise it could be possible to find just a local minimum of the interference. In the next step shown in Figure 4.3d the focusing lens into the Sagnac loop is placed in that way that the incoming and outgoing beam of the Sagnac loop is still collimated. This is ~ 30cm away from the center of the loop. By moving and tilting the lens and just tilting one mirror on the screen should be again perfectly destructive interference observed. If this is not the case, repeat the previous alignment step, else proceed with the step shown in Figure 4.3e while the pump beam is overlapping with and without the lens. In this step the ppKTP crystal (pink) is inserted in the center of the Sagnac loop. Therefore the lens has to be moved ~ 0.4cm further away from the Sagnac loop. By moving and tilting the crystal a

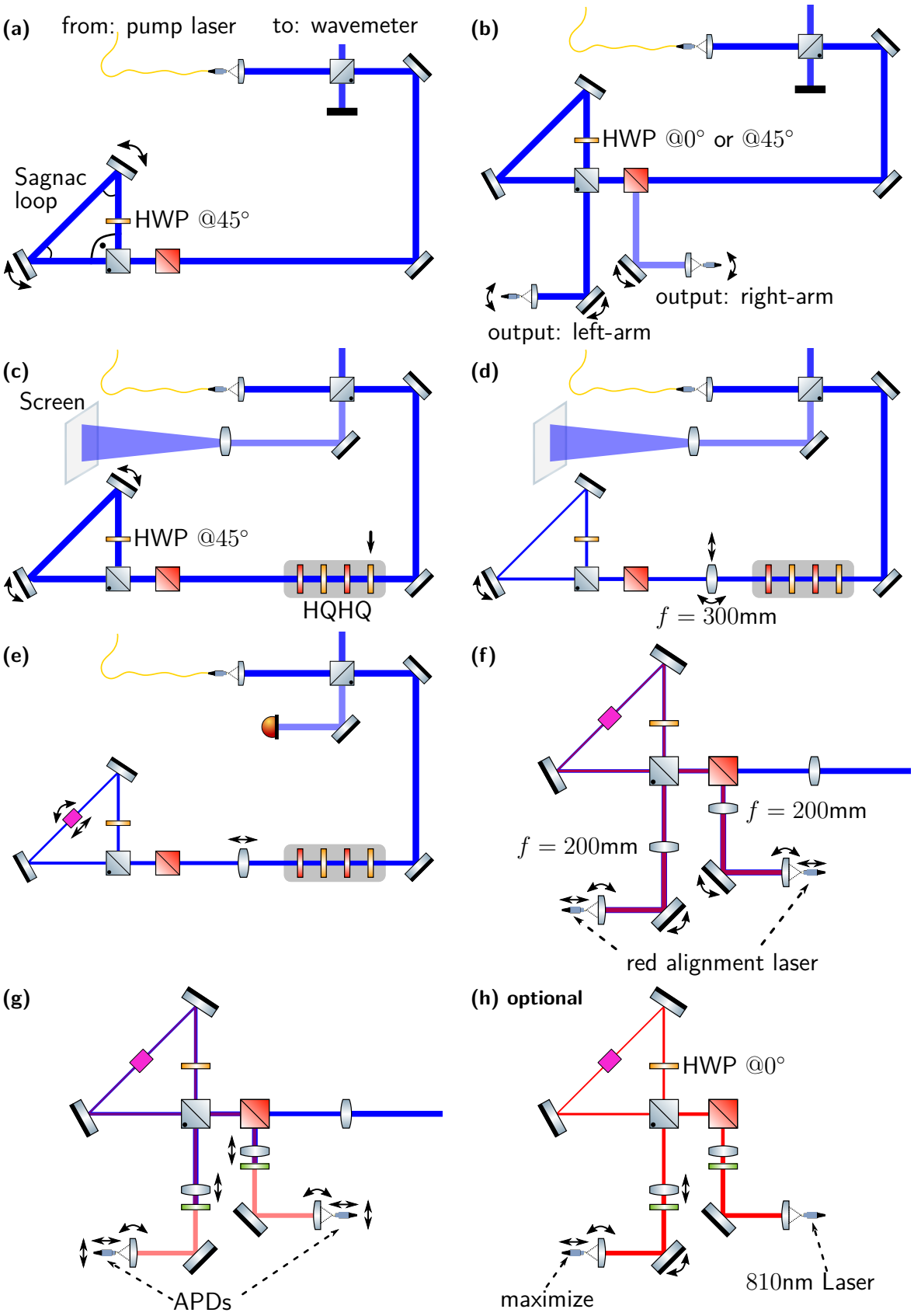

Figure 4.3: Alignment procedure for the setup shown in Figure 3.1. An explanation for every step is in the text.

perfect destructive interference can be achieved. The screen and the lens is removed and a photo diode is placed in the arm. The destructive interference is now optimised with moving the crystal forwards and backwards and tilting it as well optimising the position of the lens focusing inside the loop. Usually this is not working perfectly right from the beginning, so the procedure has to be repeated from the step shown in Figure 4.3c. It is advisable in this repeating alignment steps not to move the focusing lens towards the Sagnac loop back to its original position to also optimise this position iteratively. If the Sagnac loop is perfectly aligned with classical interference, the output arms need to be aligned as well. This is shown in Figure 4.3f where first the focusing lenses towards the crystal for the SPDC photons are placed ~ 20cm away from the crystal center. A red alignment laser is connected from the backside of the outputs. The red beam is roughly collimated. The red and blue beam is then overlapped by moving the mirrors in the output arms and tilting the coupler lens. In the last step shown in Figure 4.3g the long pass filters are inserted and the single photon detectors (APDs) are connected to the the output arms. The coupled single photon counts become maximised for each arm by moving the lenses in front of the Sagnac loop, changing the focus of the coupler itself and moving or tilting the coupler lens. If one arm couples much more than the other arm Figure 4.3h is used to shine backwards with a 810nm laser. Exemplarily shown for the worse left-arm the laser is attached to the right-arm and the half-wave plate inside the loop is turned to $0°$. The power coupled into the other arm is then maximized by changing all available degrees of freedom in this arm. Afterwards the half-wave plate inside the loop is turned back to $45°$ and the step of Figure 4.3g is repeated. If both arms have similar single counts, the photon pair counts are improved by first tuning the half-wave plate inside the loop to her perfect spot for maximal photon pair rates. Also by slightly moving the couplers the count rate can be improved. If the maximum is reached, place the plexiglass box over the entire source to ensure a stable running unaffected by rapid changes of the room temperature. After about 30min the source reaches a thermal equilibrium and the crystal temperature has changed slightly which should be compensated with the temperature controller.
After exchanging the coupler lenses the procedure has to be done again starting by Figure 4.3f. This was done every time in the same way to ensure a reproducibility of the measured values. The measured values were thereby reproducible with an uncertainty of less than 2%. In this step it is not really necessary to move the lenses focusing the coupler beam into the Sagnac-loop. It is mainly important to remove the longpass filters in the output-arms and overlap the red and blue beam again.
For measuring with the polarization analysing module it is necessary to use a polarization controller. The polarization controller is compensating any arbitrary transformation from the fiber, caused by their birefringence behaviour when twisted, to the photons polarization [39]. To achieve this a polariser in H (or V) is placed directly in front of each coupler. The measurement bases of the polarization analysing module are set up in the HV-basis. The detected counts for V (or H) shall be reduced with the help of the polarization controller until a minimum is reached. After this step the polarization analysing module can be used to measure the polarization dependencies of the photons coupled into the fiber to determine the visibility.
The visibility is adjusted with the second half-wave plate in the HQHQ by maximising the DA visibility after the setup comes inside the plexiglass box to a thermal equilibrium.

4.2 Data and Result

After the alignment has been finished first the visibility is measured by connecting the polarization analysing module to the setup and adjusting the DA-visibility as high as possible. This visibility is measured for 10 minutes. Then the basis is switched to HV in the polarization analysing module and the HV-visibility is measured for 10 minutes. If a Bell measurement is done with the CHSH inequality each of the four needed bases is also measured for 10 minutes. Afterwards the polarization analysing module gets disconnected and the detectors are directly attached to the source outputs for the brightness measurement. Therefore the pump power gets exactly adjusted on $P = 1.000$mW before each measurement and then the brightnesses are measured for 10 minutes. The heralding is calculated out of the brightness measurement.

Measurement errors

The count rates R_i are Poisson distributed. So the standard deviation is

$$\Delta R_i = \sqrt{R_i} \tag{4.2}$$

for the Poisson distributed count rates. This is the used statistical error for all values except the S and E_i values (see section 1.1.3). For the E_i values and therefore also S value the standard error is used

$$\sigma_F = \frac{\Delta F}{\sqrt{N}} \tag{4.3}$$

where N is the count of measurements which were needed to calculate the average value. The measurement interval length was 500ms for each measured value. By approximately 10 minutes measurement time for each value this makes the standard error by a factor of 35 smaller than the standard deviation.

But there are also two kinds of systematical errors in the direct evaluation of the count rates which make them bigger as they actually are. On the one hand side the detectors do not only count photons from the source but also randomly appearing clicks and other photons that get coupled randomly into the fiber. This effect is even stronger for multi mode fibers where it is much easier through the bigger core radius to get coupled in. To correct this error the pump laser gets blocked and count rates of the still appearing random counts are measured and subtracted to determine the brightness and heralding of the source. On the other hand the photon pair count rate is not free from accidental counts. For two Poisson distributed rates (R_i, R_j) that matched in a certain time window, in this measurements $t_{\mathsf{CoW}} = 1000$ps, wrong matched photon pairs $R_{\mathsf{acc.CC}}$ are appearing. Approximation to first order [40] gives:

$$R_{\mathsf{acc.CC},i,j} = R_i \cdot R_j \cdot t_{\mathsf{CoW}} \tag{4.4}$$

These accidentals are subtracted from the directly measured photon pair count rates to calculate then the visibility, the brightness and the heralding. For the adjusted power this gives approximately 25 to 75 photon pairs per second depending on how many single photons are measured. This fits well with experimentally observation by using totally wrong time offsets

for the photon pairs observation with 10 to 30 photon pairs for just a half second.

Error propagation

The visibility, brightness and heralding are all indirectly measured observables. So their error has to be calculated. If a value g depends on N different variables $a_1, a_2, ..., a_N$, the uncertainty of the value $g(a_1, a_2, ..., a_N)$ can be calculated out of the uncertainty Δa_i of the variables a_i. Therefore Gaussian propagation of uncertainty is used to calculate

$$\Delta g = \sqrt{\sum_{i=1}^{N} \left(\Delta a_i \frac{\partial g}{\partial a_i} \right)^2} \tag{4.5}$$

For the brightness (eq. (3.5)) the error is

$$\Delta B_i = \sqrt{\left(\frac{\Delta P}{P} \right)^2 + \left(\frac{\Delta R_i}{R_i} \right)^2} \cdot B_i \tag{4.6}$$

where the uncertainty of the laser power is the clearly dominant term.
The error of the average single count rate (eq. (3.6)) is:

$$\Delta R_{\text{Avg}} = \frac{1}{2} \sqrt{(\Delta R_{\text{left}})^2 + (\Delta R_{\text{right}})^2} \tag{4.7}$$

For the average heralding (eq. (3.9)):

$$\Delta \eta_{\text{Avg}} = \frac{\sqrt{4 \cdot R_{\text{left}} \cdot R_{\text{right}} + (R_{\text{left}} + R_{\text{right}}) R_{\text{CC,left,right}}^2}}{2 \cdot R_{\text{left}} \cdot R_{\text{right}}} \tag{4.8}$$

For the visibility (eq. (3.13)):

$$\Delta V_{i,j} = 2 \cdot \sqrt{\frac{(R_{\text{CC},i,j} + R_{\text{CC},j,i})(R_{\text{CC},i,i} + R_{\text{CC},j,j})}{(R_{\text{CC},i,j} + R_{\text{CC},j,i} + R_{\text{CC},i,i} + R_{\text{CC},j,j})^3}} \tag{4.9}$$

For the uncertainty of the heralding in Equation (4.8) and the visibility in Equation (4.9) Equation (4.2) was directly used to simplify the equation.

4.2.1 Brightness

The brightness is measured for the single photons and the photon pairs by observing their count rates by a fixed laser power.
The result for the single photons is shown in Figure 4.4. More single photons are coupled into the fiber for longer focal lengths of the coupler lenses. The lens pair with the longest focal length had a problem with coupling in the left-arm. The lenses were swapped between both

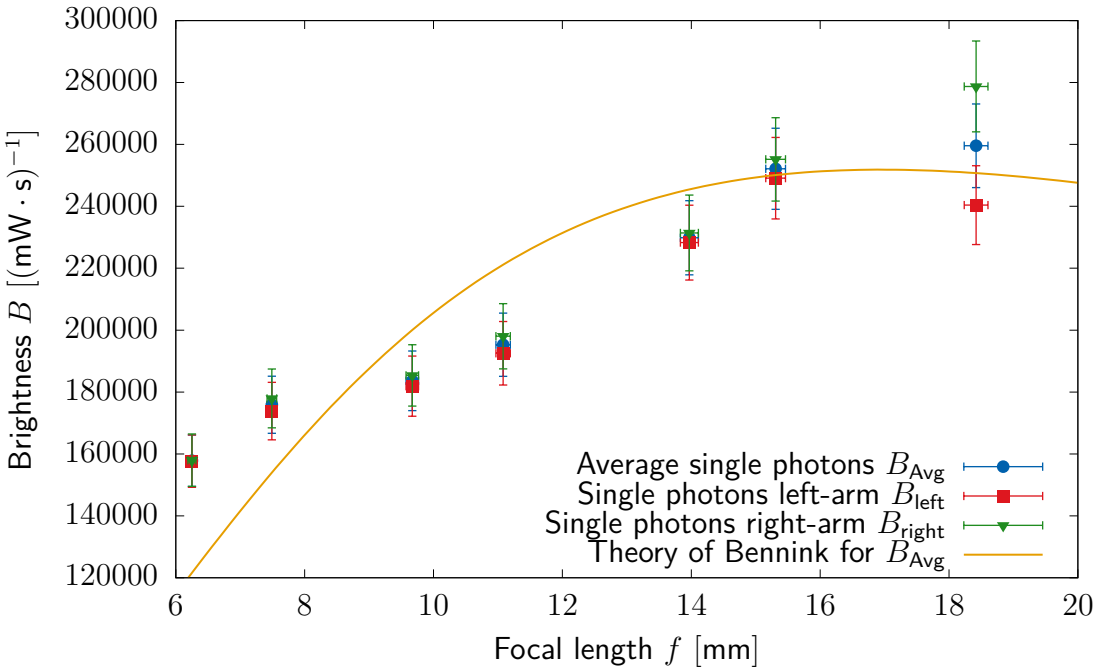

Figure 4.4: Measured brightness B of single photons coupled in each arm by a laser power of $P = 1.000\mathrm{mW}$ for different coupler focal length f over a duration of $10\mathrm{min}$ after adjusting the visibility in DA as high as possible. The average over both arms is calculated according to Equation (3.6) and is fitted with a least square fit of Equation (3.18).

arms to exclude a manufacturing error of the one lens which was first in the left-arm. The reason for this bad coupling in just one arm could not be discovered. By excluding the last lens the slope is close to a linear behavior. The strange behavior of the lens pair with the longest focal length gives a first indication to the expected worse quantum properties of the produced photon pairs for longer focal lengths.
Using the theoretical available function to fit the curve with a least-square the measured values follow that curve to a certain point and so the theory can explain the strange behaviour of the lens pair with the longest focal length because the mode overlap is simply just not possible anymore. In comparison to the theory the first two short lenses are also coupling more than expected. The next three lens pairs couple less than from the theory expected. But overall the values are showing the from the theory expected ascending behaviour and stagnation at the highest point.
The result for the photon pairs is seen in Figure 4.5. Again more photon pairs are observed for longer focal lengths of the coupler lenses. An exception is the longest lens where this statement does not hold because the less coupled single photons in the left-arm are correlating with less observed photon pairs. For the focal length between $6\mathrm{mm}$ and $11\mathrm{mm}$ the photon pairs brightness rises in a straight manner. On the brightness level of the $11\mathrm{mm}$ focal length lens the brightness is stagnating.
Using the theoretical available values for a least-square fit the results with the stagnating rise of the brightness can be explained with a expected maximum for $13\mathrm{mm}$ where it shall decrease afterwards. Again the first two lenses lying above the from the theory expected values while the next three are below the predicted values. Overall the experimental measured behaviour is similar to the theoretical predicted values except that the maximum is not there where it should be which is displaying the hard problem in finding the focal parameters for a bright

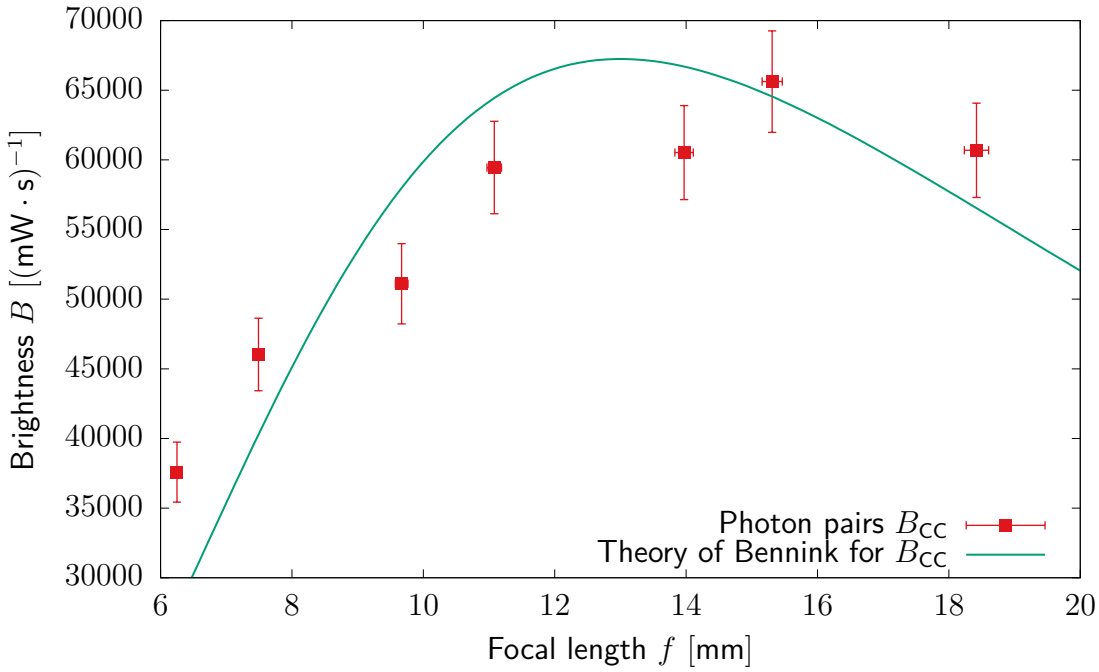

Figure 4.5: Measured brightness B of photon pairs by a laser power of $P = 1.000$mW for different coupler focal length f over a duration of 10min after adjusting the visibility in DA as high as possible. The brightness is fitted with a least square fit of Equation (3.19).

source with just using the theory. Because the highest brightness for photon pairs is not the expected one but the assumption that the best brightness is in the superposition of single photon brightness and photon pair brightness is correct.

Primarily the interest is in the high brightness of the source. Therefore a comparison of the brightness of the coupled single photons B_{Avg} and photon pairs B_{CC} is necessary to determine a first set of lenses for the desired characteristica of the source. In Figure 4.6 the single photon rates are comparable with the pair rates. In the range 11mm to 19mm is the photon pair rate stagnating. In comparison to the photon pair rates the single photon rates are still increasing. With the single photon's brightness cap of $245000/(\mathrm{mW}\cdot\mathrm{s})$ (see eq. (4.1)) the longer focal length lenses are close to this limit and the longest focal length pair is with its right-arm above that limit. Therefore the main interest relys on the lenses with the labeled focus length 11.00mm, 13.86mm and 15.29mm which have high brightness in single photons and photon pairs.

4.2.2 Heralding

The heralding of the source for the different focus parameters according to Equation (3.9) can be directly calculated from the count rates of the brightness measurement. The result in Figure 4.7 is showing that the best heralding is expected for the $f = 11.00$mm coupler lens. The theory expects for this lens a heralding of $\eta_{\mathrm{theory}} = 81.5\%$ without taking the efficiencies in the fit into account. Using Equation (3.8) and the detector efficiency of 66% the transmission loss τ can be calculated under the assumption that the theoretical heralding prediction holds. The value is $\tau = 56.6\%$ which is a typical value for a type-II source coupled into a single mode

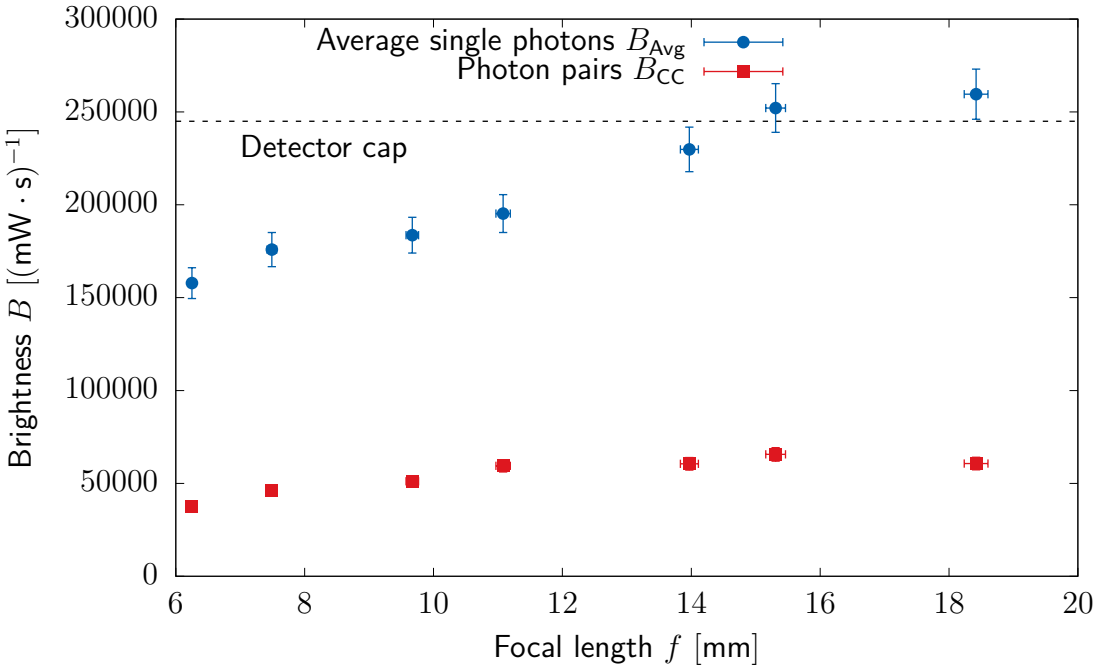

Figure 4.6: Measured brightness of the average single photons B_{Avg} of both arms and photon pairs B_{CC} by a laser power of $P = 1.000$mW for different coupler focal length f over a duration of 10min after adjusting the visibility in DA as high as possible. The wanted brightness caped for the maximum power by the efficency of the detectors.

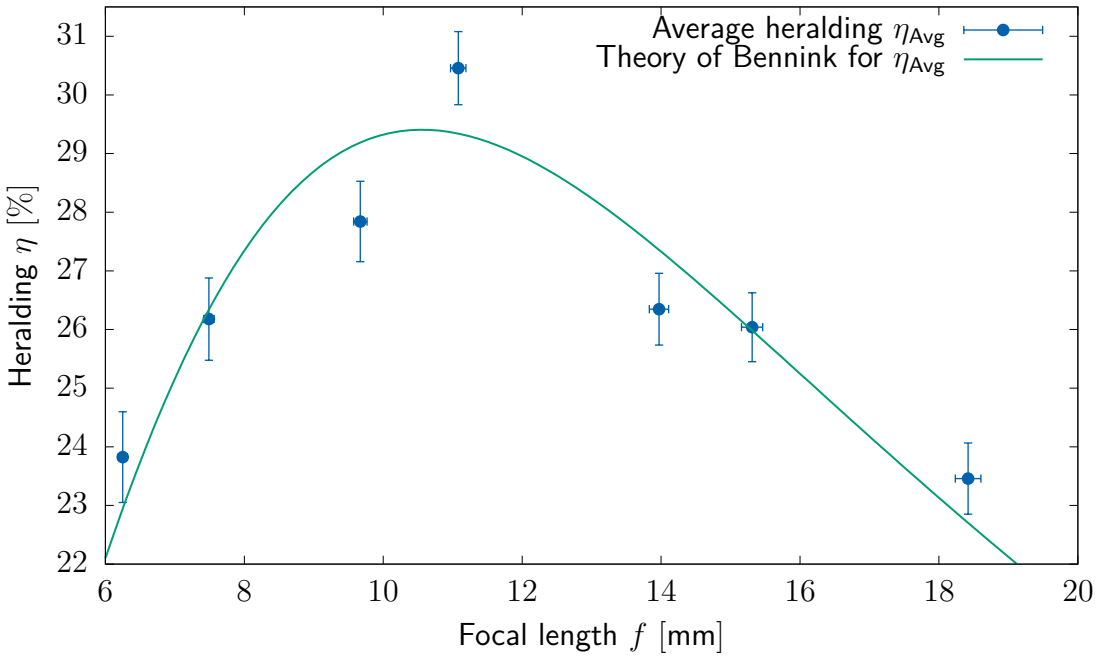

Figure 4.7: Calculated heralding η_{Avg} according to Equation (3.9) out of the values from the brightness measurement of the single photons B_{Avg} and photon pairs B_{CC} by a laser power of $P = 1.000$mW for different coupler focal length f over a duration of 10min after adjusting the visibility in DA as high as possible. The heralding is fitted with a least square fit of Equation (3.20).

fiber (see present overview [35]). For shorter focal length the heralding is increasing stronger, as it is decreasing from the highest point towards longer focal lengths.
With the theoretical available function a least-square fit is done. This function shows how well this theory can predict values for a good heralding because the highest value for the heralding measured is also obtained for the value the theory predicts. For the fit of the theoretical functions two parameters ($C1 = 1$ for the focus of the SPDC photon and $C2 = 1$ for the focus of the pump beam) were introduced. After evaluating all three functions with equal $C1$ and $C2$ their values are $C1 = 1.005 \pm 0.054$ and $C2 = 1.007 \pm 0.078$. This means the focus parameters are known with less than 1% deviation while the error of that deviation is ten times that big. This small inaccuracy can be caused by the alignment or the exact knowledge about the crystal's specifications. The deviation of the used approximation for the Gaussian beam is one magnitude smaller. Therefore this may not be an issue for the deviation and the much bigger deviation leads to the conclusion that the theory is still not complete. The last value which is from interest is the normation constant N_η which is expected to be $N_\eta = 1$ if the theory is correct. The obtained constant $N_\eta = 1.007 \pm 0.014$ has less than 1% deviation from the expected value while the error is twice that much. Therefore it can be concluded that the theory is just in a well match with the obtained experimental results in predicting the maxima and the trend. To achieve an entire match with the theory at least one additional term is necessary in the theory.

4.2.3 Visibility

The visibility is measured for the different focal lengths with the help of the polarization analysing module in HV-basis and DA-basis. The result is stated in Figure 4.8. As expected

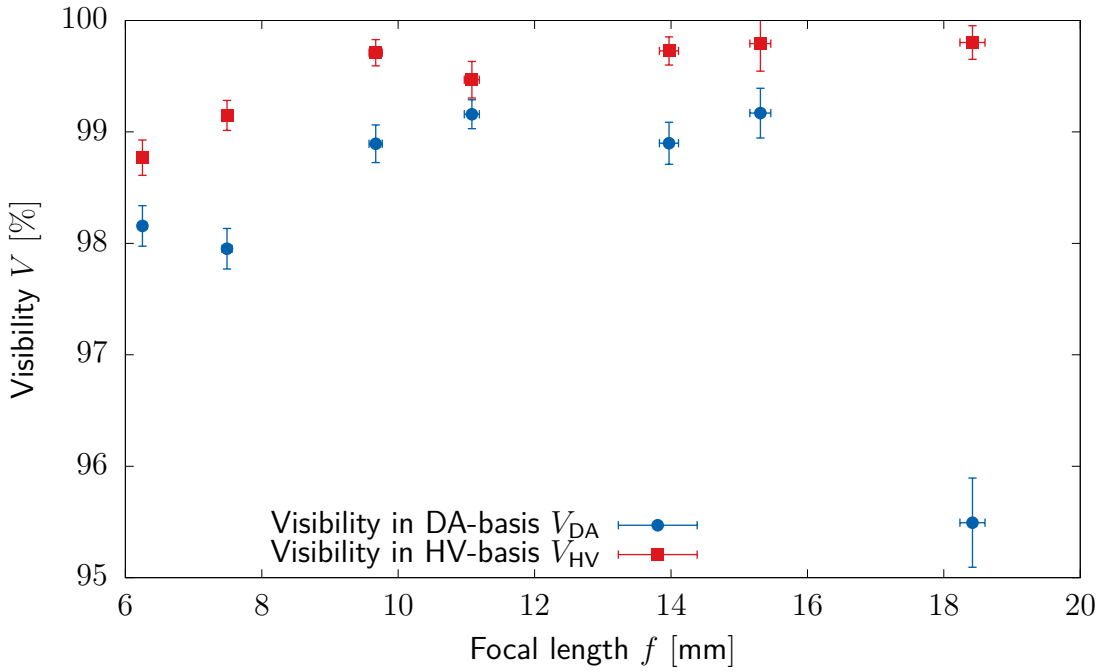

Figure 4.8: Measured visibility V of detected photon pairs in HV-basis and DA-basis by a laser power of $P = 1.000$mW for different coupler focal length f over a duration of 10min after adjusting the visibility in DA as high as possible.

the visibility in HV is always higher than in DA because the source is creating the photon in a Typ-II process so it should exist a photon of the orthogonal polarization in the opposite mode and the HV-visibility should be always close to 100%. For the longer focal lengths the visibility in HV is continuously over 99.5% and acting as expected. For the first two focal lengths the visibility is slightly worse. This can be explained with the deviation of focal parameters from the ones which are expected to be good. These lens pairs are not from interest for further investigations in a high brightness source because the other lenses have clearly better visibilities and photon pair entanglement properties than the other lenses.
The visibility in DA is for the longest focal length far away from being acceptable. This could be caused by the already bad alignment behaviour for their brightness. For the other four lenses the DA-visibility is between 0.4% and 0.8% lower than the HV-visibility. This lies exactly in range of the alignment of the Sagnac loop with a classical visibility of about $1:200$. It shows that the entanglement of the photon pairs are mainly connected with the loss of knowledge in which path direction they entered the Sagnac loop.
From the viewing point of the visibility in DA-basis of the photon pairs, which is the quick measurement tool for the quality of the entanglement, the lenses from $f = 9$mm to $f = 16$mm are from interest for a good source. A correlation which should be mentioned is that those three excluded values are those three values where the measured brightness is higher than the theoretical predicted brightness. So the assumption can be made that a from the theory expected not perfect mode overlap lowers the entanglement properties of the source.

Bell test

To give a certain proof that the created photon pairs are entangled a Bell test is made for the three best lenses ($f = 11.00$mm, $f = 13.86$mm, $f = 15.29$mm). Therefore each output arm of the source is send to a measurement party. The left-arm to the party Alice and the right-arm to the party Bob. These two parties can choose their measurement bases individually. At first Alice measures twice in the HV-basis while Bob changes his basis first to B1-basis and second to B2-basis. Secondly Alice measures again twice in the DA-basis while Bob stays in B2-basis and changes then back to B1-basis. In Section 1.1.3 the maximal possible violation

Lens f/mm	$E_1 = V(\text{DA}, \text{B1})$	$E_2 = V(\text{DA}, \text{B2})$
11.00	0.73749 ± 0.00013	0.70404 ± 0.00013
13.86	0.69945 ± 0.00016	0.70588 ± 0.00019
15.29	0.70420 ± 0.00037	0.68629 ± 0.00030

Lens f/mm	$E_3 = V(\text{HV}, \text{B1})$	$E_4 = V(\text{HV}, \text{B2})$
11.00	0.71544 ± 0.00014	-0.65409 ± 0.00014
13.86	0.76648 ± 0.00012	-0.64753 ± 0.00019
15.29	0.72394 ± 0.00025	-0.70096 ± 0.00035

Table 4.2: Result of the four expectation values with their standard error for a Bell test by violating the CHSH inequality. Each measurement lasts for about 10min.

.

of the CHSH inequality for the different E_i bases choices are presented with $S = 2\sqrt{2}$. In polarization angles the first basis for HV is $0°$, DA is $45°$, B1 is $22.5°$ and B2 is $67.5°$. The second bases are their orthogonal counterpart ($+90°$). These bases can be measured by

the polarization analysing module also used for the visibility measurement. By choosing the visibility as correlated minus anti-correlated outcome the visibilities for not identical bases in the visibility measurement are presenting the different E_i. These bases for each measurement party are adjusted in the polarization analysing module where both orthogonal polarizations simultaneously measured for 10min. The results are in Table 4.2.
By applying this values to the CHSH inequality the

$$S = V(\mathsf{HV}, \mathsf{B1}) - V(\mathsf{HV}, \mathsf{B2}) + V(\mathsf{DA}, \mathsf{B1}) + V(\mathsf{DA}, \mathsf{B2}) \leq 2 \tag{4.10}$$

values are calculated. The results are in Table 4.3. All three values for the different lens pairs

Lens f/mm	S	$S/(2\sqrt{2})$ [%]	n_σ
11.00	2.81106 ± 0.00027	99.385	3058
13.86	2.81934 ± 0.00033	99.678	2453
15.29	2.81539 ± 0.00064	99.539	1279

Table 4.3: Calculated S values with the results of Table 4.2 using Equation (4.10) for different coupler lens focal lengths, S divided by the Tsirelson's bound and the amount of standard errors of the S value to the classical limit $S = 2$.

violating the CHSH-inequality. The source is therefore producing an entangled state. The violation could be achieved with one lens pair with over 3000 σ_S. During the measurement of the $f = 15.29$mm lens the source was not quite stable caused by thermal fluctuations in the environment. This experimental setup is not in anyway loophole free (see section 1.1.3) but it is an easy way to demonstrate the entanglement properties of a source. The values are divided by the Tsirelson's bound $(2\sqrt{2})$, which is just reachable with pure maximally entangled Bell states [10]. With over 99% for the relation the created photon pairs are close to the maximally entangled $|\Psi^-\rangle$ Bell state and the source is for sure a source of polarization-entangled photon pairs.

4.3 Best result

The results for all lenses are presented in Table 4.4. The parameter for which a focal length has to be discarded is first the visibility in DA. For lenses lower 98% in V_{DA} exists no interest (values in red color). For the further lens selection $f = 7.49$mm and $f = 18.42$mm are out. The main interest was in a high brightness. With longer focal length also the brightness increases for single photons as well as for photon pairs. The cap in single photon brightness comes from the available laser pump power to conduct the noiseresilient free-space high dimensional non-local interference experiment with a desired high resolution in time. The lens with the highest available brightness matches perfectly with the requirements of $245000/(\mathsf{mW} \cdot \mathsf{s})$. So the decision was made to use the $f = 15.31$mm lens pair for the couplers because the heralding is with $\eta = 26\%$ acceptable and also higher as original ($\approx 20\%$ [1]) before an improvement attempt was made. An alternative lens pair is the $f = 11.08$mm which provides the highest heralding $\eta = 30\%$ and fulfill the equation of Bennink for the optimal spectral density of the SPDC-photons as the closest lens pair. These two lenses are marked green in Table 4.4. By combining the heralding and brightness between the original source (20%, $15\,10^3/(\mathsf{mW} \cdot \mathsf{s})$)

f_{chrom} [mm]	$B_{\text{Avg}} \cdot 10^3$ [$\text{mW}^{-1} \cdot \text{s}^{-1}$]	$B_{\text{CC}} \cdot 10^3$ [$\text{mW}^{-1} \cdot \text{s}^{-1}$]	η_{Avg} [%]	V_{DA} [%]	V_{HV} [%]
6.25	157.8 ± 8.3	37.6 ± 2.2	23.82 ± 0.77	98.16 ± 0.13	98.77 ± 0.11
7.49	175.9 ± 9.2	46.0 ± 2.6	26.18 ± 0.70	97.95 ± 0.13	99.15 ± 0.10
9.67	183.6 ± 9.6	51.1 ± 2.9	27.84 ± 0.69	98.89 ± 0.12	99.71 ± 0.10
11.08	195 ± 10	59.5 ± 3.3	$\mathbf{30.46} \pm 0.62$	99.16 ± 0.10	99.50 ± 0.12
13.97	229 ± 11	60.5 ± 3.4	26.35 ± 0.61	98.90 ± 0.13	99.73 ± 0.10
15.31	252 ± 13	$\mathbf{65.6} \pm 3.6$	26.04 ± 0.59	99.17 ± 0.16	99.79 ± 0.20
18.42	259 ± 13	60.7 ± 3.4	23.46 ± 0.61	95.49 ± 0.28	99.80 ± 0.11

Table 4.4: Overview of all measured results for the different lenses with chromatic corrected focal length f_{chrom}. B_{Avg} is the brightness of the single photons averaged over both arms, B_{CC} is the brightness of the photon pairs, η_{Avg} is the average heralding over both arms, V_{DA} is the visibility in DA-basis and V_{HV} is the visibility in DA-basis. The best results for either brightness or heralding are marked green.

and the optimised source (26%, $66\,10^3/(\text{mW}\cdot\text{s})$) the optimised source is a factor 4.4 brighter and a factor 1.3 more heralding efficient. Taking the limitation of the linear range of the detectors for single photons into account the source is factor 5.7 better than original by just optimising the focus parameter. The theory also predicts that the lens pair $f = 11.08$mm should have the highest heralding. In terms of the photon pair brightness the theory predicts a different result. The lens pair $f = 13.97$mm should give a better result than the $f = 15.31$mm but this could not be observed. The highest observed brightness for single photons and photon pairs is in between the theoretical prediction for single photons and photon pairs. In terms of predicting high brightness the theory of Bennink is not so precise as for high heralding.

Visibility curve of the chosen lens pair

The visibility curve is measured for the chosen best lens pair, while one basis was fixed either in HV or in DA and the other basis was rotated over time by the motorized half-wave plate in the polarization analysing module (see section 4.1.1) with a low angular velocity. For a maximally entangled Ψ^- state Equation (1.18) predict a sinusoidal curve for the visibility. This curve is fitted while the amplitude of these fit gives the visibility in HV or DA with $V_{\text{HV}} = (99.327 \pm 0.018)\%$ and $V_{\text{DA}} = (99.138 \pm 0.015)\%$. The phase difference between the sinusoidal curve is $\Delta\phi_{\text{left}} = (43.327 \pm 0.018)^\circ$ which means the two bases are not perfectly set up. The maximal violation of the S values is calculated by numerically maximising the S value for the two obtained curve fits and calculating the error with Equation (4.5). Thereby $S = 2.81261 \pm 0.00034$ can be obtained for the two shown angles $\phi_{\text{B1}} = 19.165^\circ$ and $\phi_{\text{B2}} = 71.630^\circ$ in Figure 4.9. For the reason that the bases are not perfectly mutual unbiased and the fact that the visibility in HV is slightly better than DA, the maximally violating spot is slightly off from the crossing point at B1 where you would naturally expecting it. This is why the value is little bit worse than the before obtained value by a direct measurement (see table 4.3) but the amount of standard errors is with 2387 σ_S a factor of two better than the direct measurement.

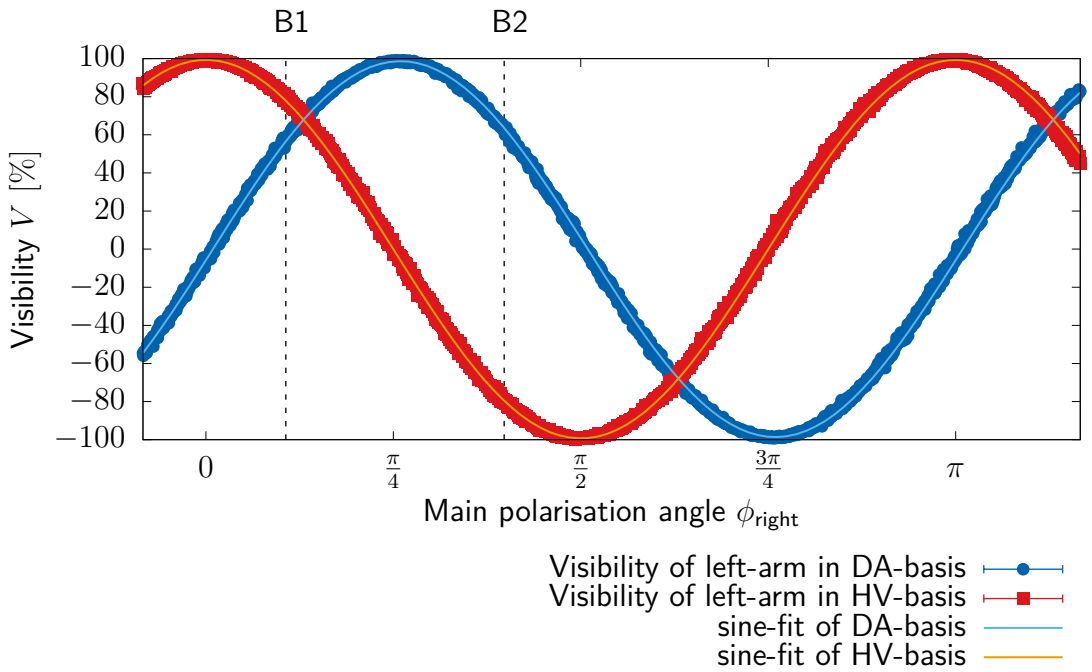

Figure 4.9: Visibility curve for the left-arm in HV ($\phi_{\text{left}} = 0°$) or DA ($\phi_{\text{left}} = 45°$) by moving the half-wave plate in the polarization analysing module for the right-arm with a slow angular velocity $\omega = 0.1°/\text{s}$. The main polarization angle is the angle of polarization in which the photons are detected for the not reflected arms in the polarization analysing module (see fig. 4.1).

4.3.1 Long term stability of best result

To obtain the long term stability over days of the chosen lens pair the different quantities are measured. The wavelength of the pump beam was measured. The wavelength was in free running and by changes over 0.0002nm pump laser's wavelength was manually adjusted. This was just three times necessary. Because of safety reasons it is not possible to run a heating device over longer time periods without being directly physical present so the laser was not locked during the three days of measurement. Also the room temperature was measured directly above the plexiglass box as well as inside the plexiglass box in the center of the Sagnac loop with a second temperature sensor. Two photo diodes were used. One of them measured the power of the laser by using the arm into the potassium stabilisation cell which was not in use and the other one measured the power in the destructive output port of the first polarized beamsplitter inside the source setup. The power was again adjusted to be 1.000mW at the standard position as before in the brightness measurements. For measuring the visibility the polarization analysing module was used as before. To determine the HV as well as the DA visibility simultaneously the bases were periodically switched with a script for the motorized half-wave plates. To enable a clear post selection the visibility V_{DA} was measured as indicated by Equation (3.13) with $V(\text{DA}, \text{DA})$ for 30s. Then the basis was switched for measuring V_{HV} but instead of turning both half-wave plates in the same orientation the half-wave plates were rotated in opposite direction and the actually $V(\text{HV}, \text{VH}) = -V_{\text{HV}}$ was measured for 20s. This enables a clean post selection by defining a threshold of over 90% for DA and lower -90% for HV. Every period is averaged and is taken as a single data point in the curve. Initially

the visibility was adjusted to be over 98.5%. After one day of measurement the polarization controller between the source and the polarization analysing module was realigned.
By analyzing the results in Figure 4.10 a periodic change was obtained which was strongly correlated with the room temperature. The polarization controller as well as the fiber in between

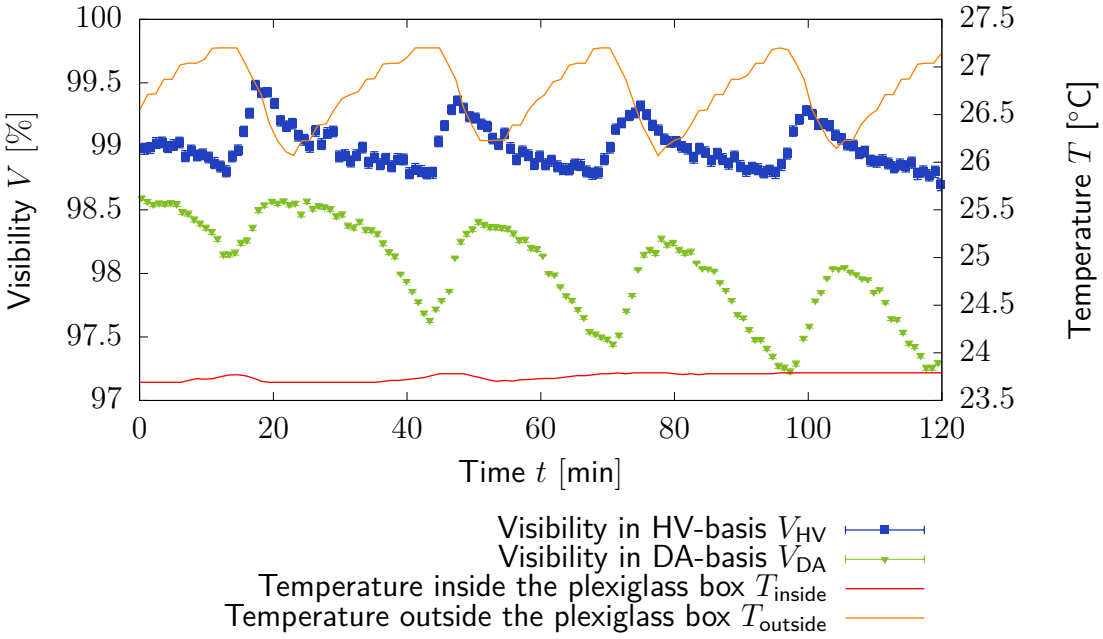

Figure 4.10: First two hours of the long term visibility measurement after realigning the polarization controller. visibility scale on the left side and temperature on the right side.

the polarization analysing module and the source are exposed to the changes of the room temperature. Thermal changes introducing different thermal stresses and thereby changes in polarization [39]. The visibility following this short term trend of the temperature. Therefore a Fourier transformation of the outside temperature curve is done. The Fourier transformation clearly indicates the period time of 24min. To compensate this effect the visibilities are averaged over the time periods of 24min. Because the visibilities are already averaged values the error bars used in Figure 4.11 are not showing the uncertainty but the minimum and maximum values present in a time period. The visiblities are lower than previously measured without changing the bases where the pump laser was also locked to the hyperfine structure. This effect was already observed while the source was built and is probably caused by the reason that the source is built and aligned for just the one special narrow wavelength. Also the temperature is averaged over 24min.
The temperature curve has two break points. After 7h the room temperature was rising by 0.7K. After 62h the room temperature was falling by again 0.7K. Comparing the visibilities at those times with the temperature curve this strong change in the temperature affects also the visibilities. After the 7h when the temperature starts rising the visibility in HV is dropping much quicker than before. This is caused by stronger thermal misalignment than before the temperature has start rising. The temperature inside the plexiglass box followed the temperature outside the box with a slow response to the outside temperature. During this time the DA visibility is rapidly changing. This could be introduced by thermal stresses inside the Sagnac interferometer's optics. Because the misalignment was so strong the polarization controller were realigned at this point. After the realignment the temperature remained for over 35h

on the same mean level. The misalignment of the polarization controller were thereby much slower and also the DA visibility was not so strongly fluctuating than before. After 62h the room temperature was falling by 0.7K. This time the visibility was not falling much quicker as before instead the polarization controller seems to undo the previous caused thermal misalignment when the temperature is changed in the other direction. Also the DA visibility benefits from this recovery of the polarization control. The temperature inside the source again is corresponding slow to the outside changes. From those slow responses of the inside temperatures to the outside temperatures it is possible to conclude that plexiglass box is well isolating the source from the outside environment and the source can run for three days without let the visibility drop below 96% while the major drops are caused by the misalignment of the fibers between detector and source itself.

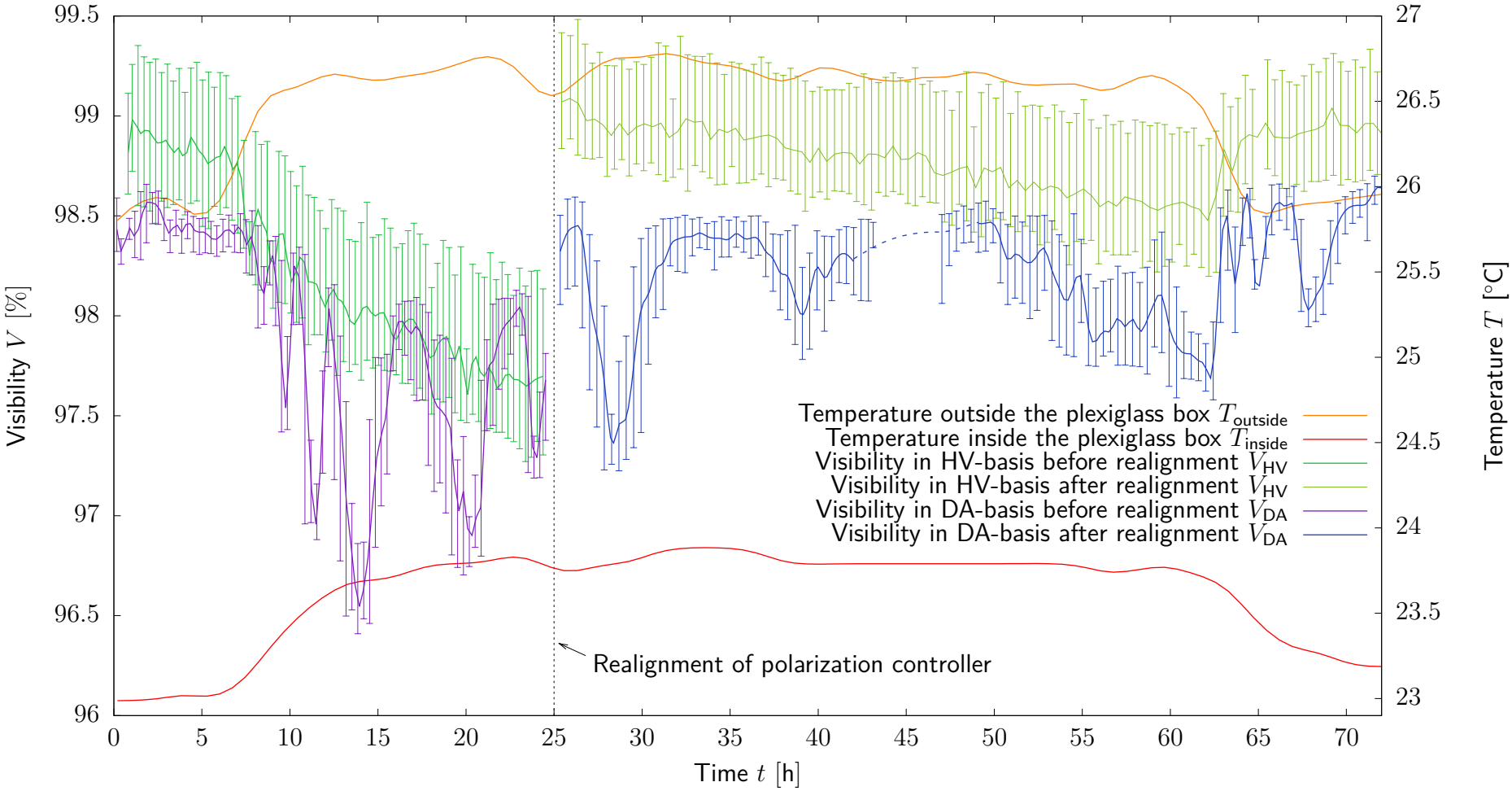

Figure 4.11: Long term visibility measurement over 72h with polarization controller realignment after 25h. Simultaneous measurement of the visibilities in HV and DA and temperature inside and outside the plexiglass box. Visibility scale on the left side and temperature on the right side. The error bars are showing the minimal and maximal values of short term viewing period which removes the short period thermal drift.

Chapter 5

Conclusion

This master thesis accomplished a way to build a narrow bandwidth high brightness type-II photon pair source with a crystal of 30mm length. From a set of available lenses, the source is optimized for a high brightness of the photon pairs without generating too many single photons (see section 4.3). A very interesting aspect is the high heralding of the source. The much higher heralding compared to the previous source parameter shows the great advantage of Bennink's theory in terms of heralding.
The used theory (see section 3.3.1) to optimise the source for brightness is a good prediction for the heralding. The theory models for optimal brightness lead closely to the maximum value findings in Section 4.2. This can be caused by different alignments as well as inaccurate laser power measurements distributed over several days. Therefore the measured brightness curves are in good agreement with actually observed values. This leads to the conclusion that optimising focus parameters for brightness is not just a mathematical problem of solving the equation. Additionally it requires to test different parameters to find the best result. This source is entirely fulfilling the requirements given by the free-space setup (see. chapter 2) by using the available pump laser power in the optimal way.
The assumption does not hold, that more photon pairs are coupled into the fiber for longer focal lengths. The theory is predicting a decrease at some point which is observed. This can be explained with boundary condition of the optical fiber which are weaker satisfied for longer focal lengths. The related assumption does hold that the quality of the quantum state is dropping for longer focal lengths.
The selected Lenses achieved a high visibility of 99% in the HV-basis as well as in the DA-basis. A proof for the generation of maximally entangled states are given by a Bell test (see section 4.2.3) where the Tsirelson's bound could be reached up to 99.5%. This bound could be theoretically just reached with perfect Bell states. Long term measurements (see section 4.3.1) showed that these high visibilities can sustain over 72h by adjusting the polarization compensation every 24h. This opens the possibility to do daylight quantum key distribution over long time periods.

All these highly tuned source characteristics where necessary to approach a noiseresilient free-space high dimensional non-local interference experiment under daylight conditions. This brightness improvement was the last necessary part which made possible an alignment over 10km before the sunrise can contribute a high number of stray-light counts.

Outlook

The source is also degenerate in wavelength and could be also useful for other applications like Hong–Ou–Mandel interference where absolute indistinguishable photons are required [41]. If someone finds a way for more available power for the SPDC process by optimising the shape of the pump laser or just increasing the laser's power the source has an alternative configuration. A pair of lenses exists with those the amount of actual available measured photon pairs can be optimised in the relation to the maximal detectable photons.

The source surpass the expectation of the initial considered improvement which allows it to use it also for different usage than the designed for. For a next experiment this source is already in use for single copy purification where a high visibility and heralding of the source is essential.

Appendix A

Bibliography

[1] Sebastian Ecker, Frédéric Bouchard, Lukas Bulla, Florian Brandt, Oskar Kohout, Fabian Steinlechner, Robert Fickler, Mehul Malik, Yelena Guryanova, Rupert Ursin, and Marcus Huber. Overcoming noise in entanglement distribution. *Phys. Rev. X*, 9:041042, Nov 2019. URL: https://link.aps.org/doi/10.1103/PhysRevX.9.041042.

[2] Ryan S. Bennink. Optimal collinear gaussian beams for spontaneous parametric down-conversion. *Phys. Rev. A*, 81:053805, May 2010. URL: https://link.aps.org/doi/10.1103/PhysRevA.81.053805.

[3] Alessandro Fedrizzi. *Fundamental experiments with a high brightness source of entangled photons*. PhD thesis, Universität Wien, Fakultät für Physik, 2008.

[4] Fabian Steinlechner. *Sources of photonic entanglement for applications in space*. PhD thesis, Universitat Politècnica de Catalunya, Institut de Ciències Fotòniques, 2015. URL: http://hdl.handle.net/2117/96057.

[5] Norman Hodgson and Horst Weber. *Laser Resonators and Beam Propagation*. Springer New York, 2005. URL: https://doi.org/10.1007/b106789.

[6] Michael A. Nielsen and Isaac L. Chuang. *Quantum Computation and Quantum Information: 10th Anniversary Edition*. Cambridge University Press, 2010.

[7] A. Einstein, B. Podolsky, and N. Rosen. Can Quantum-Mechanical Description of Physical Reality Be Considered Complete? *Physical Review*, 47(10):777–780, May 1935.

[8] J. S. Bell. On the einstein podolsky rosen paradox. *Physics Physique Fizika*, 1:195–200, Nov 1964. URL: https://link.aps.org/doi/10.1103/PhysicsPhysiqueFizika.1.195.

[9] John F. Clauser, Michael A. Horne, Abner Shimony, and Richard A. Holt. Proposed experiment to test local hidden-variable theories. *Phys. Rev. Lett.*, 23:880–884, Oct 1969. URL: https://link.aps.org/doi/10.1103/PhysRevLett.23.880.

[10] B. S. Cirel'son. Quantum generalizations of bell's inequality. *Letters in Mathematical Physics*, 4(2):93–100, March 1980. URL: https://doi.org/10.1007/bf00417500.

[11] J.S. Bell. *Speakable and Unspeakable in Quantum Mechanics: Collected Papers on Quantum Philosophy*. Collected papers on quantum philosophy. Cambridge University Press, 2004. ISBN 9780521523387.

[12] Philip M. Pearle. Hidden-variable example based upon data rejection. *Phys. Rev. D*, 2: 1418–1425, Oct 1970. URL: https://link.aps.org/doi/10.1103/PhysRevD.2.1418.

[13] Jonathan Barrett, Daniel Collins, Lucien Hardy, Adrian Kent, and Sandu Popescu. Quantum nonlocality, bell inequalities, and the memory loophole. *Phys. Rev. A*, 66:042111, Oct 2002. URL: https://link.aps.org/doi/10.1103/PhysRevA.66.042111.

[14] Christopher Gerry and Peter Knight. *Introductory Quantum Optics*. Cambridge University Press, 2004.

[15] Robert W. Boyd. *Nonlinear Optics* -. Elsevier, Amsterdam, 2008. ISBN 978-0-080-48596-6.

[16] Kiyoshi Kato and Eiko Takaoka. Sellmeier and thermo-optic dispersion formulas for ktp. *Appl. Opt.*, 41(24):5040–5044, Aug 2002. URL: http://ao.osa.org/abstract.cfm?URI=ao-41-24-5040.

[17] D. Y. Zhang, H. Y. Shen, W. Liu, G. F. Zhang, W. Z. Chen, G. Zhang, R. R. Zeng, C. H. Huang, W. X. Lin, and J. K. Liang. The thermal refractive index coefficients of 7.5mol% nb:ktiopo4 crystals. *Journal of Applied Physics*, 86(7):3516–3518, 1999, https://doi.org/10.1063/1.371251. URL: https://doi.org/10.1063/1.371251.

[18] Mirdit Doda, Marcus Huber, Gláucia Murta, Matej Pivoluska, Martin Plesch, and Chrysoula Vlachou. Quantum key distribution overcoming extreme noise: simultaneous subspace coding using high-dimensional entanglement, 2020, arXiv:quant-ph/2004.12824.

[19] Julio T. Barreiro, Nathan K. Langford, Nicholas A. Peters, and Paul G. Kwiat. Generation of hyperentangled photon pairs. *Phys. Rev. Lett.*, 95:260501, Dec 2005. URL: https://link.aps.org/doi/10.1103/PhysRevLett.95.260501.

[20] Paul G. Kwiat. Hyper-entangled states. *Journal of Modern Optics*, 44(11-12):2173–2184, 1997. URL: https://www.tandfonline.com/doi/abs/10.1080/09500349708231877.

[21] Thomas Brougham and Stephen M. Barnett. Information communicated by entangled photon pairs. *Phys. Rev. A*, 85:032322, Mar 2012. URL: https://link.aps.org/doi/10.1103/PhysRevA.85.032322.

[22] Kristian Hjorth. Using photon entanglement as a fundamental resource in experimental physics. Master's thesis, Norwegian University of Science and Technology, 2019.

[23] Jan K. Lang et al. Evaluation algorithms. *Work in progress*, 2021.

[24] J. D. Franson. Bell inequality for position and time. *Phys. Rev. Lett.*, 62:2205–2208, May 1989. URL: https://link.aps.org/doi/10.1103/PhysRevLett.62.2205.

[25] D. V. Strekalov, T. B. Pittman, A. V. Sergienko, Y. H. Shih, and P. G. Kwiat. Postselection-free energy-time entanglement. *Phys. Rev. A*, 54:R1–R4, Jul 1996. URL: https://link.aps.org/doi/10.1103/PhysRevA.54.R1.

[26] Sijin Wu, Xiaoyuan He, and Lianxiang Yang. Enlarging the angle of view in michelson-interferometer-based shearography by embedding a 4f system. *Appl. Opt.*, 50(21):3789–3794, Jul 2011. URL: http://ao.osa.org/abstract.cfm?URI=ao-50-21-3789.

[27] Taehyun Kim, Marco Fiorentino, and Franco N. C. Wong. Phase-stable source of polarization-entangled photons using a polarization sagnac interferometer. *Phys. Rev. A*, 73:012316, Jan 2006. URL: https://link.aps.org/doi/10.1103/PhysRevA.73.012316.

[28] Alessandro Fedrizzi, Thomas Herbst, Andreas Poppe, Thomas Jennewein, and Anton Zeilinger. A wavelength-tunable fiber-coupled source of narrowband entangled photons. *Opt. Express*, 15(23):15377–15386, Nov 2007. URL: http://www.opticsexpress.org/abstract.cfm?URI=oe-15-23-15377.

[29] H. R. Kratz. The principal series of potassium, rubidium, and cesium in absorption. *Phys. Rev.*, 75:1844–1850, Jun 1949. URL: https://link.aps.org/doi/10.1103/PhysRev.75.1844.

[30] Oskar Kohout. Masterthesis. *Work in progress*, 2021.

[31] R. Clark Jones. A new calculus for the treatment of optical systemsi. description and discussion of the calculus. *J. Opt. Soc. Am.*, 31(7):488–493, Jul 1941. URL: http://www.osapublishing.org/abstract.cfm?URI=josa-31-7-488.

[32] Percy Risberg. A revision of the term systems for nai and ki based on hollow-cathode observations. *Arkiv for Fysik*, 10(6):583–605, 1956.

[33] Alexandra Behrle, Marco Koschorreck, and Michael Köhl. Isotope shift and hyperfine splitting of the 4 s to 5 p transition in potassium. *Physical Review A*, 83(5):052507, 2011.

[34] Philip E. Ciddor. Refractive index of air: new equations for the visible and near infrared. *Appl. Opt.*, 35(9):1566–1573, Mar 1996. URL: http://ao.osa.org/abstract.cfm?URI=ao-35-9-1566.

[35] Ali Anwar, Chithrabhanu Perumangatt, Fabian Steinlechner, Thomas Jennewein, and Alexander Ling. Entangled photon-pair sources based on three-wave mixing in bulk crystals, 2020, `arXiv:quant-ph/2007.15364`.

[36] Alexander Ling, Antía Lamas-Linares, and Christian Kurtsiefer. Absolute emission rates of spontaneous parametric down-conversion into single transverse gaussian modes. *Phys. Rev. A*, 77:043834, Apr 2008. URL: https://link.aps.org/doi/10.1103/PhysRevA.77.043834.

[37] Christian Kurtsiefer, Markus Oberparleiter, and Harald Weinfurter. High-efficiency entangled photon pair collection in type-ii parametric fluorescence. *Phys. Rev. A*, 64:023802, Jul 2001. URL: https://link.aps.org/doi/10.1103/PhysRevA.64.023802.

[38] Daniel Ljunggren and Maria Tengner. Optimal focusing for maximal collection of entangled narrow-band photon pairs into single-mode fibers. *Phys. Rev. A*, 72:062301, Dec 2005. URL: https://link.aps.org/doi/10.1103/PhysRevA.72.062301.

[39] I. Kaminow. Polarization in optical fibers. *IEEE Journal of Quantum Electronics*, 17(1): 15–22, 1981.

[40] J. A. Grieve, R. Chandrasekara, Z. Tang, C. Cheng, and A. Ling. Correcting for accidental correlations in saturated avalanche photodiodes. *Opt. Express*, 24(4):3592–3600, Feb 2016. URL: http://www.opticsexpress.org/abstract.cfm?URI=oe-24-4-3592.

[41] C. K. Hong, Z. Y. Ou, and L. Mandel. Measurement of subpicosecond time intervals between two photons by interference. *Phys. Rev. Lett.*, 59:2044–2046, Nov 1987. URL: https://link.aps.org/doi/10.1103/PhysRevLett.59.2044.

Appendix B

Mathematica code

Bennink's paper

Definitions:

$k_p = 2\pi n_p/\lambda_p$

$k_s = 2\pi n_s/\lambda_s$

$k_i = 2\pi n_i/\lambda_i$

$\xi_p = L \Big/ \left(k_p w_p^2\right)$

$\xi_s = L \,/ (k_s w_s^2)$

$\xi_i = L \,/ (k_i w_i^2)$

$\Delta\mathbf{k} = -m * 2\pi/\Lambda$

$A_+ = 1 + (k_s \xi_s) \,/\, (k_p \xi_p) + (k_i \xi_i) \,/\, (k_p \xi_p)$

$B_+ = (1 - \Delta\mathbf{k}\,/k_p) * (1 + ((k_s + \Delta\mathbf{k})\,\xi_p) \,/\, ((k_p - \Delta\mathbf{k})\,\xi_s) + ((k_i + \Delta\mathbf{k})\,\xi_p) \,/\, ((k_p - \Delta\mathbf{k})\,\xi_i))$

$A_s = 2\sqrt{\frac{k_i\left(1+\frac{k_s \xi_s}{k_p \xi_p}\right)}{k_p}}$

$B_s = 2\left(1 - \frac{\Delta\mathbf{k}}{k_p}\right)\sqrt{\frac{(\Delta\mathbf{k}+k_i)\left(1+\frac{(\Delta\mathbf{k}+k_s)\xi_p}{(-\Delta\mathbf{k}+k_p)\xi_s}\right)}{-\Delta\mathbf{k}+k_p}}$

$A_i = 2\sqrt{\frac{k_s\left(\frac{k_i \xi_i}{k_p \xi_p}+1\right)}{k_p}}$

$B_i = 2\left(1 - \frac{\Delta\mathbf{k}}{k_p}\right)\sqrt{\frac{(\Delta\mathbf{k}+k_s)\left(\frac{\xi_p(\Delta\mathbf{k}+k_i)}{\xi_i(k_p-\Delta\mathbf{k})}+1\right)}{k_p-\Delta\mathbf{k}}}$

Results

Singles probability :

$$\frac{1}{2}\left(\frac{64\pi^3 ce\mathbf{h}\chi_{\mathbf{eff}}^2 n_i n_s \mathbf{NP}_p \tan^{-1}\left(\frac{B_i \xi_i}{A_i}\right)}{\varepsilon_0 A_i B_i \lambda_i^2 n_p \lambda_s^2 n_{\mathbf{si}'}} + \frac{64\pi^3 ce\mathbf{h}\chi_{\mathbf{eff}}^2 n_i n_s \mathbf{NP}_p \tan^{-1}\left(\frac{B_s \xi_s}{A_s}\right)}{\varepsilon_0 A_s B_s \lambda_i^2 n_p \lambda_s^2 n_{\mathbf{si}'}}\right)$$

Coincidences probability :

$$\frac{\mathbf{ArcTan}[(B_+\ \xi_s \xi_i)/(A_+ \xi_p)]\left(64ec\mathbf{h}\pi^3 n_i n_s \mathbf{NP}_p \chi_{\mathbf{eff}}^2\right)}{n'_{\mathbf{si}} A_+ B_+ n_p \varepsilon_0 \lambda_i^2 \lambda_s^2}$$

Own calculations

Definitions

$\lambda_i = \lambda_s$

$\lambda_s = 2 * \lambda_s$

$w_i = w_s$

Numerical

$m = 1$

$\Lambda = 10\text{^}(-6) * 9.86$

$L = 10\text{^}(-3) * 30$

$n_p = 1.865$

$n_s = 1.761$

$n_i = 1.887$

$\lambda_p = 10\text{^}(-9) * 404.414$

$w_p = C2 * 10\text{^}(-6) * 45.45$

$c = 1$

$e = 1$

$\mathsf{h} = 1$

$\varepsilon_0 = 1$

$\chi_{\mathsf{eff}} = 1$

$\mathsf{NP}_p = 1$

$n'_{\mathsf{si}} = 1$

$w_s = C1 * 10\text{^}(-6) * 100 * 5 / f(\text{*mm*})$

Results

Single photon rate:

$$\frac{5.55529\times10^{17}\tan^{-1}\left(\frac{8.05816f^2\sqrt{\frac{7.288176737999998^{*\wedge}\text{-}12\text{C1}^2}{\text{C2}^2f^2}+2.8960761201961405^{*\wedge}\text{-}13}}{\text{C1}^2\sqrt{\frac{2.0657025^{*\wedge}\text{-}9\cdot\text{C2}^2f^2}{\text{C1}^2}+2.5^{*\wedge}\text{-}7}}\right)}{\sqrt{\frac{7.288176737999998^{*\wedge}\text{-}12\cdot\text{C1}^2}{\text{C2}^2f^2}+2.8960761201961405^{*\wedge}\text{-}13}\sqrt{\frac{2.0657025^{*\wedge}\text{-}9\cdot\text{C2}^2f^2}{\text{C1}^2}+2.5^{*\wedge}\text{-}7}}+\frac{5.96247\times10^{17}\cdot\tan^{-1}\left(\frac{7.50786f^2\sqrt{\frac{8.395730975999998^{*\wedge}\text{-}12\cdot\text{C1}^2}{\text{C2}^2f^2}+2.8960761201961405^{*\wedge}\text{-}13}}{\text{C1}^2\sqrt{\frac{2.0657025^{*\wedge}\text{-}9\cdot\text{C2}^2f^2}{\text{C1}^2}+2.5^{*\wedge}\text{-}7}}\right)}{\sqrt{\frac{8.395730975999998^{*\wedge}\text{-}12\cdot\text{C1}^2}{\text{C2}^2f^2}+2.8960761201961405^{*\wedge}\text{-}13}\sqrt{\frac{2.0657025^{*\wedge}\text{-}9\cdot\text{C2}^2f^2}{\text{C1}^2}+2.5^{*\wedge}\text{-}7}}$$

Photon pair rate:

$$\left(\frac{1.49268\times10^{26}\cdot\text{C1}^2\text{C2}^2f^2\tan^{-1}\left(\frac{0.00792966\cdot\text{C1}^2f^2+0.000146423\cdot\text{C2}^2f^4}{\text{C1}^4+0.0165256\text{C1}^2\text{C2}^2f^2}\right)}{\text{C1}^4+0.0349909\cdot\text{C1}^2\text{C2}^2f^2+0.00030515\cdot\text{C2}^4f^4}\right.$$